Cellular/Molecular

Terminal Field and Firing Selectivity of Cholecystokinin-Expressing Interneurons in the Hippocampal CA3 Area

Bálint Lasztóczi,[1,2] **John J. Tukker,**[1] **Peter Somogyi,**[1,2] **and Thomas Klausberger**[1,2]

[1]Medical Research Council, Anatomical Neuropharmacology Unit, Department of Pharmacology, Oxford University, OX1 3TH Oxford, United Kingdom, and [2]Department of Cognitive Neurobiology, Center for Brain Research, Medical University Vienna, 1090 Vienna, Austria

Hippocampal oscillations reflect coordinated neuronal activity on many timescales. Distinct types of GABAergic interneuron participate in the coordination of pyramidal cells over different oscillatory cycle phases. In the CA3 area, which generates sharp waves and gamma oscillations, the contribution of identified GABAergic neurons remains to be defined. We have examined the firing of a family of cholecystokinin-expressing interneurons during network oscillations in urethane-anesthetized rats and compared them with firing of CA3 pyramidal cells. The position of the terminals of individual visualized interneurons was highly diverse, selective, and often spatially coaligned with either the entorhinal or the associational inputs to area CA3. The spike timing in relation to theta and gamma oscillations and sharp waves was correlated with the innervated pyramidal cell domain. Basket and dendritic-layer-innervating interneurons receive entorhinal and associational inputs and preferentially fire on the ascending theta phase, when pyramidal cell assemblies emerge. Perforant-path-associated cells, driven by recurrent collaterals of pyramidal cells fire on theta troughs, when established pyramidal cell assemblies are most active. In the CA3 area, slow and fast gamma oscillations occurred on opposite theta oscillation phases. Perforant-path-associated and some COUP-TFII-positive interneurons are strongly coupled to both fast and slow gamma oscillations, but basket and dendritic-layer-innervating cells are weakly coupled to fast gamma oscillations only. During sharp waves, different interneuron types are activated, inhibited, or remain unaffected. We suggest that specialization in pyramidal cell domain and glutamatergic input-specific operations, reflected in the position of GABAergic terminals, is the evolutionary drive underlying the diversity of cholecystokinin-expressing interneurons.

Introduction

Interconnected neuronal networks in the temporal lobe process spatial (O'Keefe and Dostrovsky, 1971; Fyhn et al., 2004) and nonspatial (Wood et al., 1999) information and encode episodic memory (Scoville and Milner, 1957; Dupret et al., 2010). This computational potential depends on spatially and temporally precise interactions between and within subnetworks of the entorhinal cortex, the dentate gyrus, and the CA3 and CA1 areas, which are responsible for different operations (Treves and Rolls, 1994; Leutgeb et al., 2004; McNaughton et al., 2006; Fyhn et al., 2007). Reflected in the behaviorally dependent neuronal oscillations (Vanderwolf, 1969; Montgomery and Buzsáki, 2007; Colgin et al., 2009), GABAergic interactions mediate a diverse set of local (Cobb et al., 1995; Klausberger et al., 2003, 2005; Mann et al., 2005; Cardin et al., 2009) and long-range (Freund and Antal, 1988; Sik et al., 1994; Jinno et al., 2007) operations, whereas glutamatergic interactions mediate information transfer between areas and local computations (Brun et al., 2002; Nakazawa et al., 2002; Nakashiba et al., 2008).

Cholecystokinin (CCK)-containing GABAergic neurons express high levels of a cannabinoid receptor (CB_1R; Katona et al., 1999) and mediate depolarization-induced suppression of inhibition in pyramidal cells (DSI; Pitler and Alger, 1992; Wilson and Nicoll, 2001). Interfering with cerebral cannabinoid signaling impairs spatial and episodic memory (Lichtman et al., 1995; Ilan et al., 2004; Rueda-Orozco et al., 2008), and the behavioral deficit is associated with abnormal neuronal oscillations and temporal coordination of firing (Hampson and Deadwyler, 2000; Robbe et al., 2006; Robbe and Buzsáki, 2009). Indeed, CB_1Rs of interneurons have been linked to mnemonic processes (Varvel et al., 2005; Puighermanal et al., 2009), and DSI has been postulated to contribute to place cell firing dynamics (Freund et al., 2003). Indi-

Received July 13, 2011; revised Sept. 26, 2011; accepted Oct. 9, 2011.

Author contributions: B.L., J.J.T., P.S., and T.K. designed research; B.L., J.J.T., P.S., and T.K. performed research; B.L., J.J.T., P.S., and T.K. analyzed data; B.L., J.J.T., P.S., and T.K. wrote the paper.

B.L. was supported by the Blaschko European Visiting Research Fellowship. This work was in part supported by Wiener Wissenschafts-, Forschungs-, and Technologiefonds (Vienna Science and Technology Fund). The help of Dr. József Somogyi with fluorescence microscopy signal detection in general and the *post hoc* bouton testing with the combination of DAB and immunofluorescent methods is highly appreciated. We also thank Ben Micklem for help with microscopy and 2D reconstructions. We thank Loránd Farkas for the reconstruction of cell J69b, István Lukács for the reconstruction of K111c, Linda Katona and István Lukács for the reconstruction of B35b, and Dr. Damien Lapray and Linda Katona for help with the reconstruction of J55d. We also thank Dr. László F. Márton for training for the reconstructions and for stimulating discussions about data analysis. The contribution of Cornelia Schimke to the 3D reconstruction of B74a is also appreciated. We are grateful to Kristina Detzner, Romana Hauer, Cornelia Schimke, and David Roberts for their excellent assistance with tissue processing. We thank Drs. Robert Stewart, Judy Creso, and László F. Márton for helping with the programming and Drs. József Csicsvári and Tim Senior for helping with tetrode recordings and clustering. We thank Dr. Katja Hartwich for providing the preparation for K111c. We are grateful to Drs. T. Görcs, R. Shigemoto, M. Watanabe, A. Varro, T. Kaneko, S. El Mestikawy, and the CURE/Digestive Research Center, Antibody/RIA Core at the University of California, Los Angeles for the gift of antibodies.

Correspondence should be sent to one of the following three authors: Bálint Lasztóczi, Department of Cognitive Neurobiology, Center for Brain Research, Medical University of Vienna, Spitalgasse 4, A-1090 Vienna, Austria, E-mail: balint.lasztoczi@meduniwien.ac.at; Peter Somogyi, Medical Research Council Anatomical Neuropharmacology Unit, University of Oxford, Oxford, OX1 3TH, UK, E-mail: peter.somogyi@pharm.ox.ac.uk; or Thomas Klausberger, Department of Cognitive Neurobiology, Center for Brain Research, Medical University of Vienna, Spitalgasse 4, A-1090, Vienna, Austria, E-mail: thomas.klausberger@meduniwien.ac.at.

J. J. Tukker's present address: Bernstein Center for Computational Neuroscience, Humboldt University of Berlin, Philippstrasse 13, 10115 Berlin, Germany.

DOI:10.1523/JNEUROSCI.3573-11.2011

 0270-6474/11/3118073-21$15.00/0

vidual CCK-expressing interneurons target distinct principal cell domains (Harris et al., 1985; Nunzi et al., 1985; Vida and Frotscher, 2000; Cope et al., 2002; Pawelzik et al., 2002; Klausberger et al., 2005) and, in this, resemble the selective innervation demonstrated for parvalbumin-expressing interneurons (Klausberger et al., 2003). In contrast to this axonal diversity, CCK-expressing interneurons in the CA1 network show surprisingly homogeneous firing characteristics with reference to oscillations *in vivo* (Klausberger et al., 2005; Tukker et al., 2007), challenging the hypothesis of cell-type-specific tasks within the CCK-expressing interneuron group. The firing patterns of CCK-expressing interneuron types in a different area may unmask their specific roles in network phenomena. Upstream of CA1, the CA3 area is involved in the generation of fast network oscillations (Csicsvari et al., 2000, 2003) and has different connectivity and a distinct role in mnemonic processes (Lee and Kesner, 2002; Nakazawa et al., 2002; Leutgeb et al., 2004). This offers an opportunity to investigate the network-specific roles of defined cell types. To test the hypothesis of distinct contributions by CCK-expressing interneuron types to network activity, we compared the firing patterns of different cell types and correlated them with pyramidal cell activity in area CA3 of urethane-anesthetized rats.

Materials and Methods

Animals. All procedures involving experimental animals were under approved personal and project licenses in accordance with the Animals (Scientific Procedures) Act, 1986 (United Kingdom) and associated regulations and with the Society for Neuroscience Policies on the Use of Animals in Neuroscience Research. Recordings were performed as described previously (Klausberger et al., 2003, 2005; Hartwich et al., 2009), with some modifications. Male Sprague Dawley rats (250–350 g) were anesthetized with urethane (1.25 g/kg body weight, i.p.) and with supplemental doses of a ketamine/xylazine mixture (20 and 2 mg/kg, i.p.) applied when necessary during the experiment. Body temperature was maintained at 37°C with a heating pad, and the electrocardiographic activity of the animal was monitored continuously.

Electrophysiological recording and labeling. Animals were placed into a stereotactic frame, a single surgical window was drilled in the skull, and the cortical surface was exposed by removing the dura mater to allow the placement of two glass electrodes (10–25 MΩ, filled with 1.5% Neurobiotin in 0.5 M NaCl) and, in some cases, an additional tetrode pair into the right dorsal hippocampus. One glass microelectrode, aimed at CA1, was inserted at −4 mm anteroposterior (AP) and 2 mm mediolateral (ML) relative to bregma, at a 20° caudal-to-rostral angle. This electrode was lowered to the stratum pyramidale, at ~2.3 mm depth, identified by large upward-going sharp waves with strong ripple oscillations and large-amplitude theta oscillations in-phase with theta oscillations recorded by another glass electrode located more dorsally, at ~1.9 mm depth (Buzsáki et al., 1986; Ylinen et al., 1995). We inserted the second glass microelectrode at a 10° rostral-to-caudal angle, at −2.8 mm AP to search for interneurons in the CA3 region. We made several tracks from 2.8 to 3.8 mm ML. Interneurons were tentatively identified based on their extracellular firing pattern using several criteria, including narrow spike width, absence of burst firing, and high firing rate (Csicsvari et al., 1999b). We tried to record and label all interneurons encountered, but data were accepted for inclusion only when the unit spikes could be unequivocally assigned to a labeled cell. Signals were referenced to either subcutaneous wire electrodes in the neck or a screw inserted above the cerebellum. The wide-band signal was divided online into unit activity (0.8–5 kHz, sampled at 20 kHz) and field potential (0.3–300 Hz, sampled at 1000 Hz; BF-48DGX and DPA-2FS signal conditioners by NPI Electronic; Power1401 A/D board by Cambridge Electronic Design) and recorded in parallel on a hard drive. A Hum-bug (Digitimer) was used to remove 50 Hz mains interference from the glass microelectrode channels. If necessary, theta oscillations were evoked by a tail pinch. After we had collected sufficient data, individual cells were approached and juxtacellularly labeled with Neurobiotin (Pinault, 1996).

Tetrodes were fabricated by twisting four 13 μm nichrome wires (enamel-coated) and were gold plated to <800 kΩ resistance. Individual tetrode channels were connected to the inputs of an acute RA16AC preamplifier (Tucker-Davies Technologies) amplified to 1000×, low-pass filtered at 6 kHz (Lynx-8; Neuralynx), and digitized at 20 kHz with the same analog-to-digital board as used for the glass microelectrode signals. Signals were referenced to a screw electrode inserted above the cerebellum. One pair of tetrodes was lowered at −3.2 mm AP and 3.1 mm ML until multiunit activity signaled the penetration into the pyramidal layer of CA3b (3.3–3.9 mm deep). For the juxtacellular recordings reported here, in two cases (experiments B34 and B35), we recorded unit activity with tetrodes in parallel. Tetrode tip positions were verified by *post hoc* histology. All data collection was controlled by Spike2 (Cambridge Electronic Design). For one of the channels used as the field potential channel, the 50 Hz interference was removed online by a Hum-Bug (Digitimer) or offline using a reference noise-method-based Spike2 script provided on Cambridge Electronic Design homepage (www.ced.co.uk).

Analysis of electrophysiological data. With the exception of gamma oscillations (see below), analyses were performed as described previously (Klausberger et al., 2003, 2005) with some modifications. Data processing and statistical analyses were done with built-in functions and scripts that we developed in Spike2 (version 7.01; Cambridge Electronic Design) and MATLAB (including the Wavelet Toolbox, version 7.9-R2009b; MathWorks). We also used some functions from the Circular Statistics Toolbox by Philipp Berens (Berens, 2009). For unit recordings with glass electrodes, we excluded periods when we observed signs that the electrode might have influenced the firing of the cell, such as large-amplitude crosstalk from unit to field potential trace, a sudden increase in firing rate, or widening of the spike.

Tetrode unit spikes were extracted from the recordings with threshold crossing (mean + 5 SD) of the root mean square (RMS) power calculated in 0.2 ms windows of bandpass-filtered (0.8–5 kHz) data (Csicsvari et al., 1998). Spikes belonging to individual units were separated by the automatic clustering software KlustaKwik (Harris et al., 2000), followed by manual refinement, separation, and merging guided by observing two-dimensional projections of feature vector cluster clouds, autocorrelograms (to obtain clear refractory periods), and cross-correlograms (to obtain no common refractory periods). For cluster refinement, we used the software Klusters (Hazan et al., 2006).

Analysis of firing associated with sharp wave/ripple complexes. The field potential from CA1 stratum pyramidale was filtered between 90 and 200 Hz (finite impulse response filter of Spike2) and the RMS power integrated in a 10 ms sliding window. Peaks of at least 5 SDs above mean were considered as putative sharp wave/ripple events. The start and end points of these were taken as the integrated power trace crossed the mean + 1 SD line; the peak identified the center. All events were checked individually and were discarded or adjusted if necessary. For time normalization of sharp wave-associated firing, spikes were binned into four equal-duration start-to-peak (−1 to 0) and four equal-duration peak-to-end (0 to +1) bins and extended for an additional 12 bins before and after the event (Klausberger et al., 2003, 2005). Note that the bin durations before or after the peak of ripple power were different in most cases because of the asymmetry of ripple events. For this analysis, sharp waves other than the one actually analyzed were removed. To calculate rate from the histogram spike counts, the values were divided by the absolute time recorded for a particular bin. For putative pyramidal cells, we recorded enough independent units to statistically assess the average changes associated with the occurrence of sharp waves. Rate values were averaged across individual units, and the statistical significance was tested with a one-way ANOVA. The change of firing rate in a bin was considered significant if it was different from at least one bin in the baseline period, either before or after the sharp wave (Bonferroni's *post hoc* comparison, $\alpha = 0.05$).

To test for correlation between firing rate variations of individual cells and sharp wave/ripple complexes, we used a temporal shuffling protocol. We intended to preserve any potential temporal structure in the spike trains; therefore, instead of randomizing the spike train, for each sharp wave, we counted the spikes in 100 sharp wave-duration windows randomly placed on a net 20 s period of the spike train centered on the event

analyzed. By limiting the window placement to this 20 s period, we controlled for the fact that the sharp waves might occur in periods associated with different baseline firing rates (e.g., theta, irregular, or slow-wave activity or transitions between these). Before shuffling, we removed all sharp waves from the train. For a sample of spike numbers from n original sharp waves, this resulted in $100 \times n$ samples of shuffled spike numbers outside sharp wave periods, which were compared by the Mann–Whitney U test at $\alpha = 0.05$. Although for convenience we report rates and not spike numbers in text, for statistical comparison, we used spike numbers to avoid potential distortions attributable to the low number of spikes, which were often 0 in any individual ~100 ms window corresponding to an event. Our shuffling design takes into account variability in the sharp wave duration.

Analysis of firing in relation to theta oscillations. Periods when the theta (3–6 Hz) to delta (2–3 Hz) power (RMS) ratio exceeded 4 or was under 2 in more than three consecutive 2 s non-overlapping windows were delineated as putative theta and non-theta–non-sharp wave periods, respectively (Csicsvari et al., 1999b; Klausberger et al., 2005). These were then segregated and adjusted manually to exclude all sharp waves and transitory periods. Unless specified otherwise, theta phase was calculated from the CA1 (stratum pyramidale) electrode. Theta troughs in 3–6 Hz bandpass-filtered traces were assigned 0° or 360° phases, and in-between phases were assigned by linear interpolation. Mean vector length and mean phases were calculated with circular statistics, and uniformity was statistically evaluated with a Rayleigh's test at $\alpha = 0.05$, unless otherwise specified (Zar, 1999). The phase-locking value (PLV; Lachaux et al., 1999) between two field potential theta oscillations was calculated as the mean vector length from the distribution of local theta troughs with respect to theta phase from CA1. The "derived CA1 mean phase" of cells was calculated by adding the CA1-to-local phase offset, i.e., the mean phase of local theta trough distribution with respect to theta phase from CA1, to the mean phase calculated with local theta as a reference.

Analysis of firing rate changes associated with brain-state transitions. To compare the firing rates of individual cells under different brain states, we took the rate detected within a single theta or non-theta–non-sharp wave period as one independent sample. Subsequent averaging over different periods provided information about both the mean rate and the temporal variance of rate over periods belonging to a particular brain state. The significance of the difference between the resulting datasets was assessed with the nonparametric Mann–Whitney U test at $\alpha = 0.01$. We only analyzed cells for which we obtained at least four periods and a minimal cumulative length of 50 s for both brain states.

Analysis of gamma oscillation associated firing. Modulation of discharge activity by gamma oscillations was separately analyzed for theta and non-theta–non-sharp wave periods. Because some CCK-expressing interneurons ceased firing completely during non-theta–non-sharp wave states, in the present study, we report data for the theta periods only. For pyramidal cells, qualitatively similar data were obtained for the non-theta–non-sharp wave periods. For removing artifacts in the local field potential caused by relatively large action potentials in the juxtacellular recordings, we substituted three to five data points (3–5 ms) of the local field potential recording around the spikes with linear interpolation values. We investigated the effect of spike artifact removal on the gamma coupling by applying the artifact removal procedure to the local field potential recorded by a tetrode containing no "spike artifacts." Comparing the mean vector length spectra and mean phase spectra (see below for the details of their calculation) of cell firing to the local field potential before and after the procedure in two experiments disclosed no effect beyond minor quantitative differences. For each spike that occurred during theta periods, we performed wavelet transformation for a wide range of frequencies (from 15 to 100 Hz; 85 logarithmically equidistant wavelet scales). A Morlet wavelet was used with wavelet parameters of 1 and 1.5 on a 2 s temporal window centered on the spike, sampled at 1 kHz temporal resolution. The instantaneous phase spectra at the spike were collected for each cell, and the data were subjected to statistical testing. Spectra of mean vector length, mean phase, and Rayleigh's z were calculated for each cell with respect to both local (various laminar locations in CA3) and reference (CA1 stratum pyramidale) electrodes. Data are displayed as normalized, color-coded spike density plots as a function of phase and frequency, which is equivalent to a stack of phase distribution histograms calculated for bandpass-filtered traces at each frequency (Le Van Quyen et al., 2001). Because the p value spectra are estimates, we report statistical significance on the basis of Rayleigh's z-spectra using a limit of 4.6052. This provides a conservative estimate of significance with $\alpha \leq 0.01$ for all cells (Zar, 1999). As a control, we calculated the significance also with p value spectra at $\alpha = 0.01$ with similar results. Cells with less than 20 spikes in theta periods were not included in the gamma analysis.

To calculate the modulation of gamma oscillation amplitude by theta oscillation phase, the field potential records were subjected to a wavelet transform as described above, the modulus values were Z-transformed for each frequency independently, the theta periods were cropped, and the Z-transformed modulus values were theta phase binned (theta phase from CA1 stratum pyramidale; 40 bins; within-bin values were averaged) and averaged across theta cycles. Phase coupling between field potentials recorded at different sites in the gamma frequency range was calculated by computing the PLV (Lachaux et al., 1999) from instantaneous phase differences between wavelet transforms downsampled to 200 Hz. The significance was assessed by estimating the 5th and 95th percentile of PLV distribution spectra calculated from 1000 shuffled (140–540 ms positive jitter introduced) wavelet transforms. This calculation also provided a mean phase offset spectrum between the two field potential traces. The calculation of the "derived CA3 stratum pyramidale mean phase spectrum" was accomplished by taking the local mean phase spectrum and adding the phase difference spectrum calculated to CA1 (to get a "derived CA1 stratum pyramidale mean phase spectrum") and subtracting a representative phase difference spectrum between CA3 stratum pyramidale and CA1 stratum pyramidale, taken from a tetrode recording.

Tissue processing, immunohistochemistry, fluorescent microscopy, and cell reconstruction. Neurobiotin was allowed to diffuse for 1–4 h into the distal compartments of the cells after labeling, while the animal was still under anesthesia. The animals were then transcardially perfused with cold saline, followed by 300 ml of cold fixative (4% paraformaldehyde, 0.05% glutaraldehyde, and 15% v/v saturated picric acid in 0.1 M phosphate buffer, pH ~7.4). Brains were removed, and sections of the right hippocampus were cut at nominally 70 μm thickness in the coronal plane with a vibratome (Leica VT 1000S).

We performed immunohistochemical reactions on individual free-floating sections to establish the protein expression in Neurobiotin-labeled interneurons. For incubations, standard procedures were used as described previously (Somogyi et al., 2004). Neurobiotin was visualized with streptavidin conjugated to Alexa Fluor 488 (1:1000; Invitrogen), DyLight488 (1:500 or 1:1000; Jackson ImmunoResearch), or 7-amino-4-methylcoumarin-3-acetic acid (AMCA) (1:100; Vector Laboratories). We used commercially available secondary antibodies raised in donkey (unless indicated otherwise) against the primary antibodies of the appropriate species, conjugated to AMCA (1:100; Vector Laboratories), Alexa Fluor 488 (1:1000; Invitrogen), DyLight488 (1:500; Jackson ImmunoResearch), Cy3 (1:400; Jackson ImmunoResearch), or Cy5 (1:250; Jackson ImmunoResearch). For the visualization and evaluation of most reactions, standard epifluorescent microscopy was used, with one of three upright microscopes. Because excitation and emission spectra of Alexa Fluor 488 and Dylight488 completely overlap, the same filter sets were used to detect the two fluorophores in separate sections. The filter sets, objectives, light source, and camera used with the Leitz DMRB microscope have been described in detail previously (Ferraguti et al., 2004; Somogyi et al., 2004). We also used an Olympus BX61 microscope with 20× (UPlanSApo, NA 0.75), 40× (oil immersion, UPlanFLN, NA 1.3), or 60× (oil immersion, PlanApoN, NA 1.42) objectives, an EXFO mercury vapor arc lamp (Lumen Dynamics) for epifluorescent illumination, filter sets U-MNUA2 (AMCA; 360–370 nm excitation bandpass, 400 nm dichroic mirror, 420–460 nm emission bandpass; Olympus), U-MNIBA3 (Alexa Fluor 488; 470–495 nm excitation bandpass, 505 nm dichroic mirror, 510–550 nm emission bandpass; Olympus), U-MNIGA3 (Cy3; 540–550 nm excitation bandpass, 570 nm dichroic mirror, 575–625 nm emission bandpass; Olympus), and U-M41008 (Cy5; 590–645 nm excitation bandpass, 660 nm dichroic mirror, 670–

730 nm emission bandpass; Chroma Technology) to separate the fluorescent light of different channels, and an Olympus XM10 monochrome cooled CCD camera controlled by Cell ^{F} software (version 3.3; Olympus) to capture images. The third microscope (Carl Zeiss AxioImager.Z1) was used for standard epifluorescent imaging, for optical sectioning with a structured illumination system (Carl Zeiss ApoTome), and for confocal laser scanning microscopy (Carl Zeiss LSM 710); it was equipped with 10× (EC Plan Neofluar, NA 0.3), 20× (PlanApochromat, NA 0.8), 40× oil-immersion (PlanApochromat, NA 1.3), and 63× oil-immersion (PlanApochromat, NA 1.4) objectives. For standard epifluorescent imaging, the light source was a software-switchable light-emitting diode set (Colibri; Carl Zeiss) with 365 nm (for AMCA), 470 nm (for Alexa Fluor 488), 530 nm (for Cy3), and 625 nm (for Cy5) diodes or a wide-band mercury vapor lamp (Xcite; EXFO). For structured illumination, the mercury vapor lamp was used for all fluorophores. Although with light-emitting diodes no excitation filters are needed, because of the hardware configuration we used the same filter sets with diodes and the lamp. Images were captured with an AxioCam HRm3 monochrome CCD camera (Carl Zeiss), controlled by the AxioImager software (Carl Zeiss), and we used the filter sets (Carl Zeiss) designed for AMCA (code 49; 365 nm excitation filter, 395 nm dichroic mirror, 445/50 nm emission bandpass), Alexa Fluor 488 (code 38HE; 470/40 nm excitation bandpass, 495 nm dichroic mirror, 525/50 nm emission bandpass), Cy3 (code 43HE; 550/25 nm excitation bandpass, 570 nm dichroic mirror, 605/70 nm emission bandpass), and Cy5 (code 50; 640/30 nm excitation bandpass, 660 nm dichroic mirror, 690/50 nm emission bandpass). For optical sectioning with structured illumination, we used the grids appropriate for the given objective (L1 for 10× and 20×, M for 40×, and H1 for 63×).

The axon terminals of basket cell K111c were tested by immunofluorescence using confocal scanning microscopic detection of antibodies. Because the axon was weakly labeled by Neurobiotin, it could not be reliably detected by fluorescence, and Neurobiotin in the terminals was detected by the horseradish peroxidase (HRP) enzyme reaction with nickel-intensified 3,3-diaminobenzidine-4 HCl (DAB) as chromogen. Fluorescence images of the same area were then matched to test for the presence of vasoactive intestinal polypeptide (VIP) and vesicular glutamate transporter type 3 (VGLUT3) immunoreactivity in the identified terminals of K111c. Image stacks were taken using an AxioImager.Z1 microscope (see above; 63× objective, LSM 710 scanning head, ZEN 5.0 software). The sequential scanning parameters were as follows: for Neurobiotin/CB_1R (Alexa Fluor 488), laser 488 nm, filter 492–544 nm, pinhole 1.0 Airy unit (AU); for VIP (Cy3), laser 543 nm, filter 552–639 nm, pinhole 0.83 AU; and for VGLUT3 (Cy5), laser 633 nm, 637–757 nm, pinhole 0.55 AU. Pixel size was 90 nm (x, y). Pinhole sizes were adjusted to produce optical slice thickness of 700 nm in each channel; optical slices were taken at 500 nm intervals. Four scan lines were averaged. The 8-bit images were noise filtered by using a Median algorithm (kernel size: $x = 3$, $y = 3$, $z = 1$, kernel size channels = 1). Because the terminals of the cell were immunonegative for VIP, there was no signal in the Cy3 channel; therefore, the signals for Neurobiotin/CB_1R (Alexa Fluor 488) and VGLUT3 (Cy5) were completely separated, and crosstalk between the detection channels was avoided.

No parts of images were modified in any way, and digital brightness and contrast adjustments were made on full frames. Although we applied standard procedures for all immunoreactions, as a result of unavoidable differences in some parameters between experiments (e.g., length of anesthesia before perfusion, quality of perfusion, number of electrode tracks made, time of storage in buffer, and the number of immunoreactions performed before the reaction), the results of immunofluorescent reactions showed some variability. Immunofluorescence signals in the Neurobiotin-labeled axonal, dendritic, or somatic compartments, as appropriate, were compared with neighboring immunopositive and immunonegative structures of similar type in the same focal plane. Care was taken that the exposure time, illuminating light intensity, and all other parameters were set to result in the correct dynamic range, so that even low-intensity signals were detected (see Figs. 3*A*, 5*A*). In most cases, after careful examination of the specimen, an all-or-none qualitative conclusion on the immunofluorescence signal associated with a particular Neurobiotin-labeled neuronal structure was possible. A Neurobiotin-labeled compartment, and as a consequence a cell, was classified "immunopositive" only if the immunofluorescence pattern was clear and its subcellular distribution was consistent with that expected, e.g., Golgi-apparatus-like for pro-CCK, nuclear for chicken ovalbumin upstream promoter-transcription factor II (COUP-TFII), or dendritic-membrane-associated for neurokinin receptor type 1 (NK_1R). A cell was classified as "immunonegative" only if it could be successfully tested for immunofluorescence in the appropriate compartment [e.g., axon for CB1R and VGLUT3, soma for CCK and COUP-TFII, soma or proximal dendrite for calbindin, and soma or dendrite for metabotropic glutamate receptor 1-α (mGluR1α)] and if neighboring non-filled cells in the same picture frame were detected as immunopositive. The specimens in which multiple immunoreactions were performed were always carefully examined by comparing the patterns observed in the different channels. Results from immunoreactions were accepted only if it was ascertained that no cross-reactivity between any of the primary and secondary antibody combinations occurred and that a reliable separation between fluorescent imaging channels had been achieved. If any of the above criteria for evaluating a reaction was not met, the reaction was considered to be inconclusive.

Publications detailing the specificity of antibodies to calbindin (rabbit, 1:5000; mouse, 1:400), CB_1R (rabbit and guinea pig, both 1:1000), CCK octapeptide (mouse, 1:5000), pro-CCK (rabbit, 1:500 or 1:5000), mGluR1α (guinea pig, 1:1000), mGluR7a (rabbit, 1:500), NK_1R (rabbit, 1:2000), prepro-tachykinin B (PPTB; guinea pig, 1:500), VGLUT3 (rabbit, 1:1000), and VIP [rabbit, 1:10000 (Dr. T. Görcs, Semmelweis Medical University, Budapest, Hungary); mouse, 1:50,000 (Dr. G. Ohning, University of California, Los Angeles, CA)] were given previously by Klausberger et al. (2005, their supplemental Table 1) and to COUP-TFII (mouse, 1:250), muscarinic acetylcholine receptor 2 (M_2R) (rat, 1:250), and VGLUT3 (guinea pig, 1:300) by Fuentealba et al. (2010, their supplemental Table 1). The specificity of the guinea pig polyclonal antibody raised against synthetic VGLUT3 peptide fragment (AB5421, 1:2000; Millipore Bioscience Research Reagents) was tested by Montana et al. (2004) in Western blot experiments. The specificity of the goat polyclonal anti-calretinin antibody (CG1, 1:1000; Swant) was tested by Western blot and by immunohistochemistry experiments (Schwaller et al., 1999). Specificity of other polyclonal antibodies used, which included antibodies raised against CCK precursor protein in guinea pig (1:500; gift from Dr. M. Watanabe, Hokkaido University, Hokkaido, Japan), against CCK octapeptide in rabbit (1:500; gift from Dr. M. Watanabe), against mouse mGluR1α peptide fragment in rabbit (1:1000; mGluR1a-Rb-Af811-1; Frontier Institute Co.), against neuropeptide tyrosine (NPY) in rabbit (1:5000; code 22940; Immunostar), and against rat NK_1R peptide fragment in rabbit (1:500, AB5060; Millipore Bioscience Research Reagents) was tested by the antibody provider, and these antibodies produced labeling patterns similar to that seen by several other previously characterized antibodies recognizing the same molecules. We also used a monoclonal mouse antibody against somatostatin (1:500, GTX71935; GeneTex) that produced labeling pattern similar to that seen with other somatostatin antibodies characterized previously.

Axonal and dendritic distributions were examined by light microscopy on sections processed with the HRP enzyme reaction for visualizing Neurobiotin using the glucose oxidase method for the generation of H_2O_2 and DAB only or nickel-intensified DAB as chromogens. The sections were osmium treated, dehydrated, and mounted on slides in epoxy resin. Two-dimensional reconstructions were made with a drawing tube with a 100× oil-immersion objective. Three-dimensional reconstructions were made with the Neurolucida software (version 9; MicroBrightField) using a 100× oil-immersion objective (Olympus UPlanFLN, NA 1.30).

Results

Recordings from identified interneurons in CA3

We recorded activity patterns of interneurons with juxtacellular electrodes in the CA3/CA2 region of the dorsal hippocampus in urethane-anesthetized rats. Sixty-seven cells, subsequently labeled with Neurobiotin (Pinault, 1996), were successfully recovered for *post hoc* histological identification. The somatic ($n = 19$), proximal dendritic ($n = 1$), or axonal ($n = 8$) compartments of 25 interneurons were tested for CCK immunoreactivity using fluorescent visualization of antibodies. In 10 cells, in which successful reactions

could be confirmed in the tissue, we did not observe detectable CCK immunoreactivity in the cell, whereas in four cells, reactions resulted in inconclusive results. The remaining 11 cells were CCK immunopositive in their soma ($n = 8$; see Figs. 1, 3*A*, 5*A*, insets), axon ($n = 2$; Fig. 2*A*, 4*A*, insets), or proximal dendrite. Ten of these cells are described in the present study, whereas one (J26c) had a long-range projecting axon (Jinno et al., 2007) and is not included here. Consistent with the correlation between the expression of CCK and CB_1R (Katona et al., 1999), all CCK-immunopositive interneurons tested ($n = 7$) were immunopositive for the CB_1R (Table 1; see Figs. 2*A*, 4*A*). Four interneurons immunopositive for CB_1R (A01a, B37b, B41c, and J06a), however, were CCK immunonegative (Bodor et al., 2005; Fuentealba et al., 2010). Other molecular markers tested were found to be differentially expressed by CCK-immunoreactive interneurons (Table 1). Interneurons expressing CCK comprise a diverse population that can be divided based on their selective axonal terminations: those in the CA1 area include basket cells, apical-dendrite-targeting cells, perforant-path-associated cells, Schaffer-collateral-associated cells, and CCK cells coexpressing COUP-TFII (Harris et al., 1985; Cope et al., 2002; Pawelzik et al., 2002; Klausberger et al., 2005; Fuentealba et al., 2010). Our sample of CCK-expressing interneurons from the CA3 area showed a comparable diversity, and we grouped them on the basis of their axonal arborization and molecular expression profile.

CCK-expressing basket cells

Basket cells, a subset of which express CCK (Harris et al., 1985; Nunzi et al., 1985; Klausberger et al., 2005; Glickfeld and Scanziani, 2006; Neu et al., 2007), innervate the soma and proximal dendrites of pyramidal cells. In the hippocampus, they can be recognized by their preferential innervation of the pyramidal layer (Ramon y Cajal, 1893; Gulyás et al., 1993; Freund and Buzsáki, 1996; Klausberger et al., 2005; Glickfeld and Scanziani, 2006; Szabadics and Soltesz, 2009; Szabo et al., 2010). Based on the axonal distribution biased to the pyramidal cell layer, we classified three CCK-immunopositive interneurons (K111c, J69b, and B68c; Figs. 1, 2*A*) as CCK-expressing basket cells. None of the axonal arbors were confined to the stratum pyramidale, but they spread into the proximal zones of stratum oriens and toward stratum lucidum/radiatum. The somata of basket cells were found in the middle (K111c; Fig. 1) or proximal part of the stratum radiatum bordering the stratum lucidum (B68c) or within the stratum lucidum itself (J69b; Fig. 2*A*). Regardless of the soma location, significant proportions of basket cell dendrites were found in all strata (Figs. 1, 2*A*; Table 1). Cell K111c had a profound dendritic tuft located in stratum lacunosum-moleculare (Fig. 1), whereas J69b (Fig. 2*A*) and B68c had fewer dendrites in this layer and more in the stratum oriens.

The two types of CCK-containing basket cells coexpress either the VGLUT3 (Somogyi et al., 2004) or the neuropeptide VIP (Acsády et al., 1996b). None of the basket cells in our sample expressed VIP at detectable levels, whereas two were immunopositive for VGLUT3, which also coexpressed mGluR1α and NK_1R in their dendritic membrane (Fig. 2*A*, inset; Table 1). Although this combination has not been found in any other interneuron type of the present sample (Table 1), additional tests on a larger sample will be necessary to establish whether the coexpression of CCK/VGLUT3/NK_1R/mGuR1α identifies a distinct set of basket cells.

CCK-expressing perforant-path-associated cells

We labeled two interneurons in the CA3a/b areas (J55d and B34b; Fig. 3) with axonal and dendritic arborizations characteristic of cells providing feedback inhibition to distal dendritic segments of pyramidal cells (Gulyás et al., 1993). Both cells had multipolar somata and complex, densely branching dendritic trees showing the highest density in the stratum radiatum, aligned to the associational inputs from the CA3 pyramidal cells, fewer dendrites in strata lucidum, pyramidale, and oriens, and no significant part of dendritic arborization in the stratum lacunosum-moleculare, in which direct inputs from the entorhinal cortex terminate (Fig. 3*A*; Table 1). The main axons emanated from the somata (Fig. 3*A*, asterisk) and gave rise to a dense axonal arborization, complementing the dendritic distribution: both cells selectively innervated the stratum lacunosum-moleculare of CA3, having no significant part of the axonal arborization in the stratum radiatum. The axon terminal field of B34b extended into the outer one-third of the molecular layer of the suprapyramidal blade of the dentate gyrus. Although the axonal features resembled those of stratum oriens lacunosum-moleculare cells in CA3 (Gulyás et al., 1993; Gloveli et al., 2005), neither of the two cells expressed mGluR1α at detectable levels (Fig. 3*A*; Table 1); J55d was immunonegative for somatostatin, and no mGluR7a-immunopositive puncta were associated with its dendrites (Fig. 3*A*), in contrast to reports for stratum oriens lacunosum-moleculare cells (Baude et al., 1993; McBain et al., 1994; Shigemoto et al., 1996). Both cells expressed CCK (Fig. 3*A*; Table 1) and CB_1R and NK_1R (Table 1), which together with the axonal and dendritic distributions identify these cells as CCK-expressing perforant-path-associated cells (Klausberger et al., 2005). Lacking axonal VGLUT3 labeling, the molecular expression profile of these cells is distinct among the present sample of CCK-containing interneurons (Table 1).

CCK-expressing dendritic-layer-innervating cells and interneurons coexpressing CCK, calbindin, and COUP-TFII

We defined two neurons as dendritic-layer-innervating cells (J45a and B74a; Figs. 4*A*, 5*A*), based on their axonal and dendritic arborizations and a lack of detectable nuclear COUP-TFII immunoreactivity (Fig. 5*A*; Table 1; see below). The cells had similar protein expression patterns (Table 1), including expression of VGLUT3 (Fig. 4*A*) in axons and NK_1R (Fig. 5*A*) in the somato-dendritic membrane, and a lack of mGluR1α immunoreactivity. These cells had large, multipolar somata close to the border between the strata radiatum and lacunosum-moleculare and varicose, sparsely branching, long dendrites extending into the termination zones of both entorhinal and associational inputs. The greater part of the dendritic length was distributed between the stratum radiatum (~65%) and stratum lacunosum-moleculare (~30%), with only few branches reaching the strata lucidum, pyramidale, or oriens (Figs. 4*A*, 5*A*). Because of the loss of one section, the very tips of three dendrites of J45a in the stratum radiatum were not included in the reconstruction in Figure 4*A*. In both cells, the main axon originated from the thickest dendrite ~20 μm from the soma and gave rise to axonal arborizations forming two distinct domains: one in the CA3 stratum radiatum/lacunosum-moleculare and the other in the molecular layer of the dentate gyrus. The cell J45a innervated the stratum radiatum of CA3a, CA3b, and CA3c, with a few branches in CA2 (the CA3c innervation is not shown in Fig. 4*A*). The border zone between strata radiatum and lacunosum-moleculare received a dense innervation, but only few axon collaterals entered the stratum lacunosum-moleculare (Fig. 4*A*). The cell B74a innervated CA3a strata lacunosum-moleculare and radiatum extensively with an increased axonal density at the border zone between the two strata (Fig. 5*A*). In the dentate molecular layer, J45a preferentially innervated the middle third of the layer (which is not seen in the two-dimensional projection in Fig. 4*A*), whereas axon of B74a distributed more

uniformly, forming a dense network in the border zone between the molecular layer and stratum lacunosum-moleculare of CA3 (Fig. 5*A*).

Approximately 50% of CCK-expressing interneurons in CA1 stratum radiatum coexpress COUP-TFII (Fuentealba et al., 2010), and these cells show a firing pattern different from that of other CCK-expressing interneurons (Klausberger et al., 2005; Fuentealba et al., 2010). In our sample in CA3, three of seven CCK-immunoreactive interneurons tested were positive for COUP-TFII (Table 1). One cell (B34b) was weakly labeled for COUP-TFII and immunonegative for calbindin and was identified as a perforant-path-associated cell. The other two cells (B35b and J38b) displayed strong nuclear COUP-TFII labeling (Fig. 6*A*) and coexpressed calbindin and CCK (Fig. 6*A*; Table 1) and were therefore grouped as interneurons coexpressing CCK, COUP-TFII, and calbindin, a scheme supported by their firing pattern being distinct from that of other cells. These two cells were located in the stratum radiatum of CA3 (B35b) and CA2 (J38b). Dendrites of the cell B35b were in strata radiatum and lacunosum-moleculare, with some extending into strata lucidum, pyramidale, and oriens (Fig. 6*A*), whereas dendrites of J38b spanned from stratum oriens to radiatum but did not enter the stratum lacunosum-moleculare to a significant extent (Table 1). The labeled axon recovered in experiment J38 could not be unequivocally assigned to either of the two separately recorded and labeled cells (J38a and J38b) and therefore it was not analyzed. The axon of B35b innervated strata oriens, pyramidale, lucidum, and radiatum, with a higher density in the proximal than in the distal part of the radiatum, and the granule cell layer of the dentate gyrus (Table 1). To test whether this cell represents an interneuron-specific interneuron making synapses exclusively onto other interneurons (Freund and Buzsáki, 1996), we randomly sampled filled boutons of the cell in stratum oriens with an electron microscopic analysis (Fig. 6*B*,*C*) and found six synapses onto dendritic shafts of putative pyramidal cells and one synapse onto a dendrite of an interneuron, and two dendritic targets could not be classified further.

We recorded and labeled another calbindin-immunopositive cell (J65a) that shared axonal and dendritic features with cells J45a and B74a, but had a markedly different protein expression pattern (Table 1). The test for COUP-TFII was inconclusive as a result of a failure of the immunoreaction, so that we did not group it with the COUP-TFII-positive cells, and for our purposes here, we refer to it as a dendritic-layer-innervating cell. Its axonal arborization spread in the stratum radiatum of CA3 with a sharp cutoff at the borders to strata lucidum and lacunosum-moleculare. There was a smaller axonal arborization in the stratum oriens of CA3b but no innervation of the molecular layer of the dentate gyrus. The dendritic distribution was similar to the other two dendritic-layer-innervating cells (Table 1).

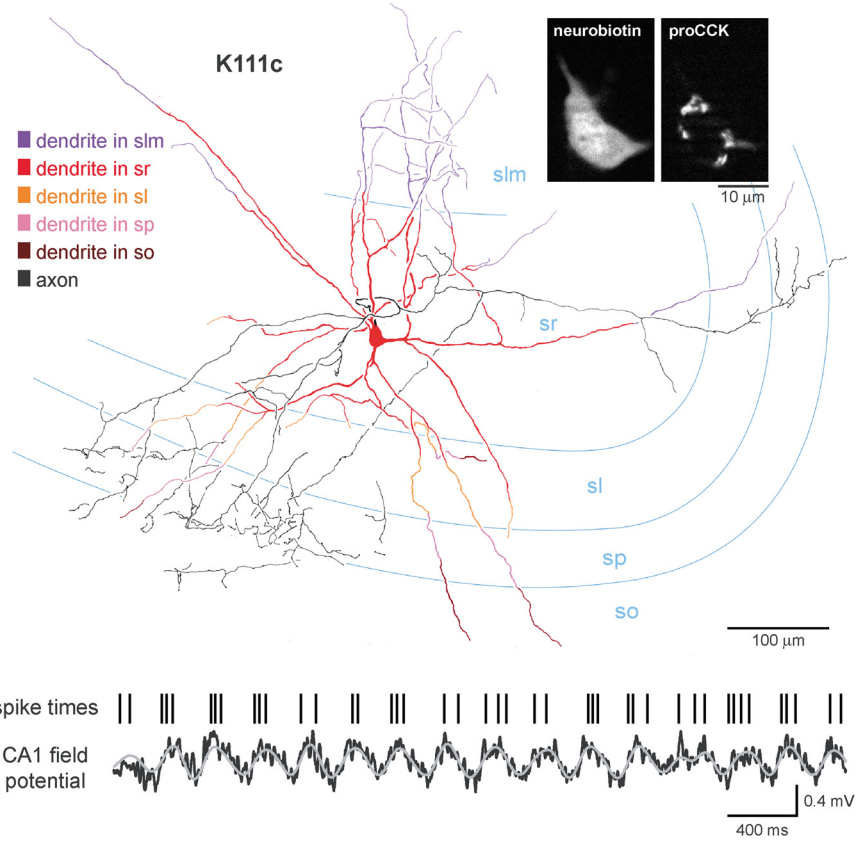

Figure 1. Visualization and theta oscillation-associated firing pattern of a CCK-containing CA3b basket cell with its soma in the stratum radiatum. Top, Two-dimensional reconstruction of the cell (K111c); the axon (black) is partially reconstructed from three consecutive sections (70 μm thickness). The main axon branches in the stratum radiatum (sr) but bouton-bearing axon collaterals are found mostly in stratum pyramidale (sp). Approximate layer boundary positions (blue) are from the section in which the boutons were recorded. The dendritic tree is reconstructed in its full extent from 12 consecutive sections. The dendrites are color coded according to the segments found in the appropriate layers (inset); because of the curvature of the hippocampus, the laminar boundaries shift in the plane of this two-dimensional view. Top right, Fluorescence visualization of the cell body demonstrating immunoreactivity for the CCK precursor protein (proCCK), in the perinuclear Golgi apparatus. Bottom, CA1 field potential (black) filtered in the theta frequency range (gray, 3–6 Hz). Vertical lines above the trace represent co-recorded spikes fired by cell K111c; the spikes preferentially occur on the late ascending phase and peak of the theta cycles. slm, Stratum lacunosum-moleculare; sl, stratum lucidum; so, stratum oriens.

Firing selectivity of interneurons during neuronal oscillations

To address how diversity of CCK-expressing interneurons may support network operations and how they may interact with the principal cells of the hippocampus, we analyzed the firing of identified interneurons and putative CA3 pyramidal cells in relation to sharp wave/ripple complexes and theta and gamma oscillations. Interneurons and pyramidal cells were recorded by extracellular glass electrodes and tetrode pairs, respectively. In 15 experiments with tetrodes in the CA3b/c region (Fig. 7*A*), we recorded 72 neuronal units, 49 of which were classified as putative pyramidal cells based on their low firing rate (0.88 ± 0.54 Hz; range, 0.14–2.4 Hz), autocorrelogram showing a bursting firing pattern (first peak of the autocorrelogram <10 ms; Fig. 7*A*), extracellular spike shape features (Csicsvari et al., 1999b; Henze et al., 2000), and occasionally by monosynaptically activating putative interneurons (Csicsvari et al., 1998).

Brain-state-dependent changes in firing rate of CA3 pyramidal cells and CCK-expressing interneurons

We compared firing rates of CA3 cells between theta periods and non-theta–non-sharp wave periods, the latter including mostly ~1 Hz oscillations corresponding to cortical up–down state fluc-

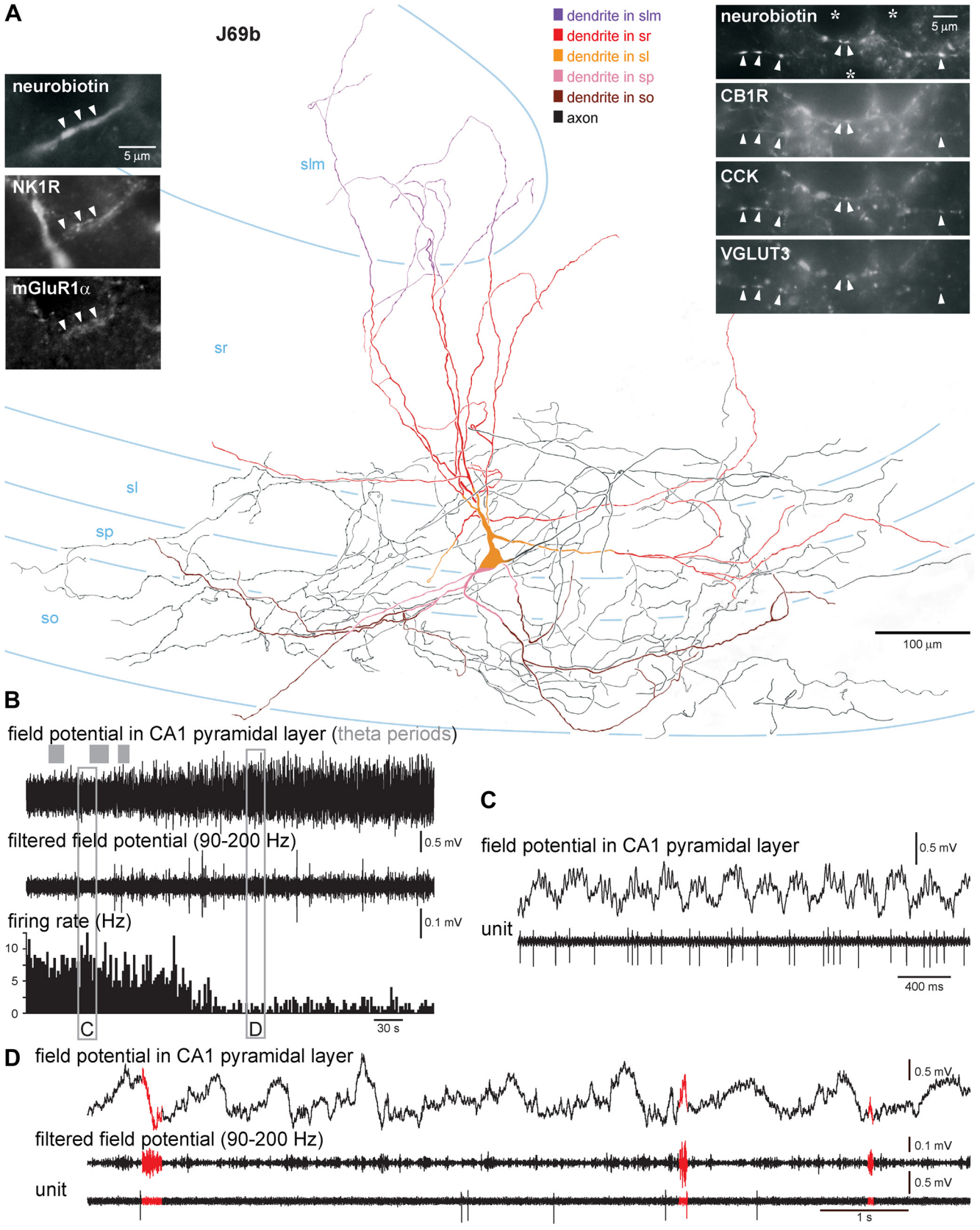

Figure 2. Visualization and firing patterns of a CCK-containing basket cell (J69b) with its soma located in stratum lucidum (sl). ***A***, Reconstruction showing the axon (black, from one 70-μm-thick section containing the soma) and dendrites (complete, 10 consecutive sections) color coded according to their laminar position; the laminar boundaries were approximated. The axon densely innervates the strata pyramidale (sp) and lucidum, along with the proximal strata radiatum (sr) and oriens (so). The left inset shows a dendritic segment (arrowheads) visualized by immunofluorescence microscopy, demonstrating weak immunoreactivity for both the NK_1R and mGluR1α. The right inset shows the Neurobiotin-filled axon in the stratum pyramidale (asterisks mark neuronal somata) and immunofluorescence for CB_1R, CCK octapeptide, and VGLUT3 in the boutons (arrowheads). ***B***, Change of the firing rate associated with changes in the brain state from theta oscillations (*Figure legend continues.*)

tuations (Isomura et al., 2006; Hahn et al., 2007). Overall, the average firing rate of pyramidal cells was not different between theta and non-theta–non-sharp wave states ($p = 0.19$; Mann–Whitney U test; $n = 49$; Table 2). Twenty-five pyramidal cells fired at similar rates between the two states; 14 fired more and 10 fired less during theta oscillations (Mann–Whitney U test, $\alpha = 0.01$). In contrast, and as for CCK-expressing interneurons of CA1 (Klausberger et al., 2005), most CCK-expressing CA3 interneurons showed intense firing when the network was in the theta state, and this was significantly attenuated during transition to the non-theta–non-sharp wave state (Table 2; $p \ll 0.01$, Mann–Whitney U test; Figs. 2*B*, 4*B*). The only exception was cell J65a, a calbindin-expressing dendritic-layer-innervating cell that fired equally slowly in both the theta and the non-theta–non-sharp wave state (Table 2; $p = 0.12$, Mann–Whitney U test).

Theta-oscillation-associated firing patterns of CA3 pyramidal cells and CCK-expressing interneurons

Although pyramidal cells were active only in ~20% of theta cycles (Table 2), their spike probability distribution with respect to theta phase was not uniform. Of 49 CA3 pyramidal cells, 46 (94%) were significantly phase locked to CA1 theta oscillations ($p < 0.05$, Rayleigh's test). The majority of the cells fired most just after the trough of theta cycles (Fig. 7*B*, black bars; nonuniform distribution of mean phases; $p \ll 0.01$, Rayleigh's test). The firing rate of the CA3 pyramidal cells fluctuated between 0.5 and 1.5 Hz, with the highest firing rate observed on the early ascending phase (Fig. 7*B*, gray circles).

Firing of individual CCK-expressing interneurons was significantly phase coupled to theta oscillations ($p \ll 0.01$ for all 10 cells, Rayleigh's test; Table 2), and as a group, they were more strongly theta phase locked than pyramidal cells (Table 2; $n = 10$; $p = 0.015$, Mann–Whitney *U test*). Theta-rhythmic, clockwork-like firing with discharges on most theta cycles (Table 2) was observed for basket cells (Figs. 1, 2*C*), perforant-path-associated cells (Fig. 3*B*), two of three dendritic-layer-innervating cells (Figs. 4*C*, 5*B*), and to a lesser extent also for COUP-TFII/calbindin cells (Fig. 6*D*). In contrast to their similar rhythmicity, the preferred theta phases of interneurons segregated in a cell-type-dependent manner (Fig. 8; Table 2). All basket cells with different soma locations (Figs. 1, 2*C*) and dendritic-layer-innervating cells (Figs. 4*C*, 5*B*) fired preferentially on the late ascending phase of CA1 theta oscillations (Fig. 8; Table 2), which is remarkably similar to the firing of CCK interneurons in the CA1 area (Fig. 8; circular mean of mean phases ± circular SD for CA3 dendritic layer-innervating and basket cells: 144 ± 11°; $n = 6$; for CA1 CCK cells, 149 ± 34°, $n = 10$; $p = 0.72$ with two-sample Watson–Williams test; Klausberger et al., 2005). Perforant-path-associated cells (Fig. 3*B*) preferentially fired on the trough/early ascending phase, matching the phase preference of pyramidal cells (Fig. 8; Table 2). This firing phase difference correlated with differences in dendritic distribution between interneuron types (Table 1). The two additional cells coexpressing COUP-TFII and calbindin fired in phase lock with the descending phase of theta oscillations (Figs. 6*D*, 8; Table 2*)*.

For the analyses above, we referenced spike timing to theta phase in CA1 stratum pyramidale. Although theta oscillations have been reported to be coherent throughout the hippocampus in both freely moving and anesthetized preparations (Buzsáki et al., 1986; Fox et al., 1986; Kamondi et al., 1998; Buzsáki, 2002; Lubenov and Siapas, 2009), we also evaluated the CA3 theta oscillations in an attempt to explore local interactions. Whenever detectable in both areas, field potential theta oscillations were coherent between the CA1 electrode and the tetrode (Fig. 7*B*; PLV, 0.81 ± 0.15, $n = 12$) or the other glass electrode in CA3 (PLV, 0.66 ± 0.21, $n = 10$). Moreover, the strength of phase coupling between spikes and CA1 or local theta oscillations was not significantly different for either pyramidal cells (Fig. 7*B*; vector length to local theta, 0.31 ± 0.12; $n = 38$ cells; $p = 0.37$; Mann–Whitney U test) or CCK-expressing interneurons as a group (mean vector length to CA1 theta, 0.45 ± 0.14; to local theta, 0.37 ± 0.17; $n = 10$; $p = 0.23$, Mann–Whitney U test). For the firing of all CA3 cells, the CA1 phase preference directly calculated, and the one deduced from the CA3 mean phase by subtracting the mean CA1-to-CA3 theta phase difference, showed strong correlation ($r = 0.97$, angular–angular correlation, $p \ll 0.01$; $n = 47$ cells; interneurons and pyramidal cells pooled). The deduced phases closely matched the directly calculated CA1 angles, resulting in all values lying around the diagonal when plotted against each other (data not shown). These results support the validity of referencing the firing of CA3 cells to CA1 stratum pyramidale theta oscillations.

Firing patterns of CA3 pyramidal cells and CCK-expressing interneurons during sharp wave/ripple complexes

To analyze the firing patterns of CA3 cells in relation to sharp wave/ripple complexes, we detected increases in the ripple power (90–200 Hz) of the field potential recorded in CA1 stratum pyramidale. Most detected events were associated with prominent slow positive deflections (sharp wave) in the wide-band signal (Figs. 2*D*, 3*C*, 4*D*, 5*C*, 7*C*), so we refer to them as sharp wave/ripple complexes or shortly as sharp waves. In CA3 pyramidal cells ($n = 40$ of 49; 82%), sharp wave/ripple complexes were associated with a significant increase in firing rate ($p < 0.05$, Mann–Whitney U test, Fig. 7C; Table 2). On average, a significant increase in the pyramidal cell population firing rate started before, persisted throughout the full duration, and ended in synchrony with CA1 sharp waves (Fig. 7*C*; $F_{(31,1536)} = 14.36$, $p \ll 0.01$ with one-way ANOVA, followed by Bonferroni's *post hoc* comparison at $p < 0.05$). Given the average duration of sharp wave/ripple complexes as ~80 ms, the offset between the increase in the CA3 pyramidal cell population rate and the CA1 sharp waves corresponds to ~10 ms, which is consistent with the population synchrony emerging in CA3 and being propagated to CA1 (Csicsvari et al., 1999a, 2000).

For two basket cells, the averages of firing rate changes associated with sharp waves did not show significant difference ($p > 0.1$, Mann–Whitney U test; Figs. 2*D*, 8; Table 2). Nevertheless, in cell B68c, the firing seemed to be suppressed for some sharp waves but not for others (Fig. 8), similar to some CCK-expressing interneurons in CA1 (Fig. 8; Klausberger et al., 2005). In contrast to this, perforant-path-associated cells were markedly activated during many sharp waves ($p \ll 0.01$, Mann–Whitney U test; Figs. 3*C*, 8; Table 2). Dendritic-

←

(*Figure legend continued.*) to irregular activity. Field potential record (CA1, top) and the same field potential filtered between 90 and 200 Hz, on a slow timescale. Theta periods by our criteria are marked by horizontal gray bars above the traces. Note the increase in the amplitude of field potential fluctuations in the unfiltered trace (see also ***C***, ***D***) and an increased incidence of high-amplitude transients (ripples) in the filtered trace. Bottom, Firing rate of the cell in 2 s bins showing a decrease associated with the brain-state transition. The approximate times of plots ***C*** and ***D*** are boxed. ***C***, Firing pattern associated with theta oscillations. Field potential (CA1, top) and unit firing (bottom) showing that the cell fires rhythmically and is coupled to the ascending phase and the peak of theta cycles. ***D***, Sharp wave-associated firing pattern. Field potential recording (top) of three sharp wave/ripple complexes (red) from CA1 showing transient increases in the amplitude of 90–200 Hz oscillations (middle trace). The firing of the cell (bottom) is not correlated with the sharp waves. Voltage calibration bar in ***C*** applies to both traces. slm, stratum lacunosum-moleculare.

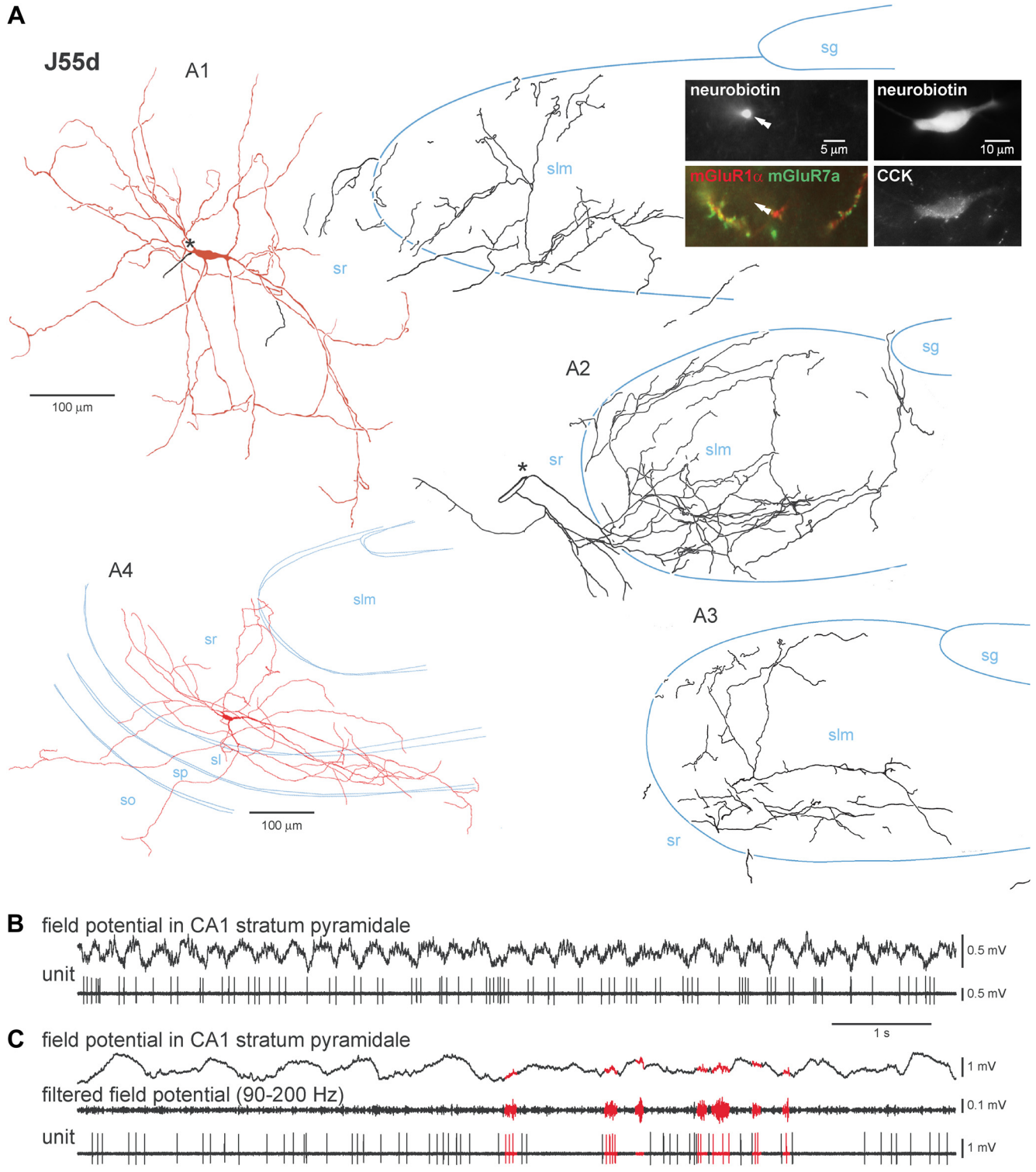

Figure 3. Visualization and firing patterns of a CCK-containing perforant-path-associated cell (J55d). ***A***, Reconstruction of the cell; the soma and dendritic tree shown in full (9 consecutive 70-μm-thick sections). The axon in ***A1*** is from two consecutive sections, including the soma and the axon initial segment (marked by an asterisk). In ***A2*** and ***A3***, the reconstruction of the axon from an additional two (***A2***) and one (***A3***) section caudal to the soma shows a highly restricted innervation of the stratum lacunosum-moleculare (slm), to a small extent of the stratum radiatum (sr), but not the dentate gyrus. In ***A4***, the three-dimensional reconstruction of the dendritic tree is shown rotated to achieve the maximum layer boundary overlap, with the average layer borders in blue. Note that very low density of dendrites is found in the stratum lacunosum-moleculare. Inset, Top left, Fluorescence visualization of a proximal dendrite (double arrowhead) showing the lack of immunoreactivity for the mGluR1α (red) and mGluR7a (green), which decorate other unidentified dendrites. The soma (top right inset) is immunoreactive for the CCK octapeptide. ***B***, Theta-oscillation-associated firing patterns. Field potential (CA1 stratum pyramidale, top) and unit firing (bottom) traces show that the cell fires rhythmically on virtually all theta cycles and is coupled to the trough of the cycles. ***C***, Sharp wave/ripple (red)-associated firing pattern. Recordings of field potential (top), the field potential filtered between 90 and 200 Hz (middle), and unit activity (bottom) during slow oscillations. The cell fires intensely during most sharp waves. The calibration bar applies to ***B*** and ***C***. sg, Stratum granulosum; sl, stratum lucidum; sp, stratum pyramidale; so, stratum oriens.

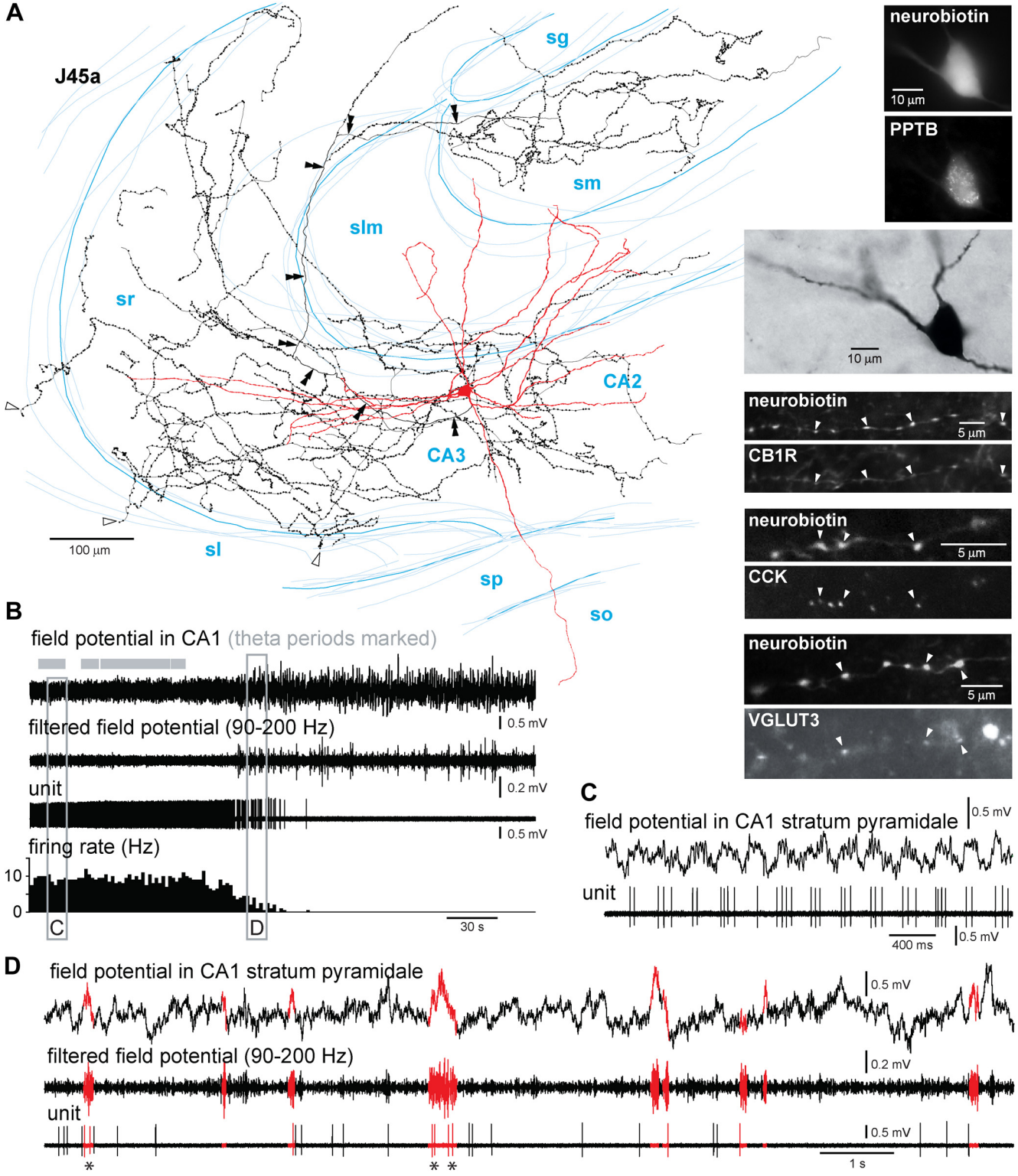

Figure 4. Visualization and firing patterns of a CCK-containing dendritic-layer-innervating cell (J45a). ***A***, Two-dimensional projection of the soma and dendrites shown in red (8 consecutive 70-μm-thick sections); the axon (black, partial from 5 consecutive sections, boutons indicated as dots) innervates mostly stratum radiatum (sr) and the molecular layer (sm) of the dentate gyrus. Note that, for better visibility, the boutons are enlarged in three-dimensional reconstructions and therefore appear larger and more numerous when compared with two-dimensional reconstructions. The projection axis of the three-dimensional reconstruction is parallel to the septo-temporal axis and was chosen to maximize the overlap of layer boundaries (thin blue lines, average thick blue line) in individual sections. The open and the double arrowheads mark the axon invading the stratum lucidum (sl) and the main axon, respectively. Insets, Immunofluorescent and DAB (black) visualizations of the same cell. The soma was immunoreactive for PPTB; the axon and boutons (arrowheads) was immunoreactive for CB_1R, CCK, and VGLUT3. ***B***, Change in the firing rate of cell J45a associated with changes in the brain state. The field potentials in the CA1 stratum pyramidale (top) and the same field potentials filtered between 90 and 200 Hz are shown on a slow timescale. Theta periods by our criteria are marked by horizontal gray bars. Bottom, The firing of the cell (unit) and the firing rate in non-overlapping 2 s bins. The brain-state transition from theta oscillations to irregular activity, which led to the complete cessation of firing, is shown by the increase in the amplitude of field potential fluctuations and the increased incidence of high-amplitude transients in the filtered trace (ripples). The approximate times expanded in plots ***C*** and ***D*** are boxed in gray. ***C***, Firing pattern of the cell associated with theta oscillation. Field potential (CA1, top) and unit firing (bottom) during (*Figure legend continues.*)

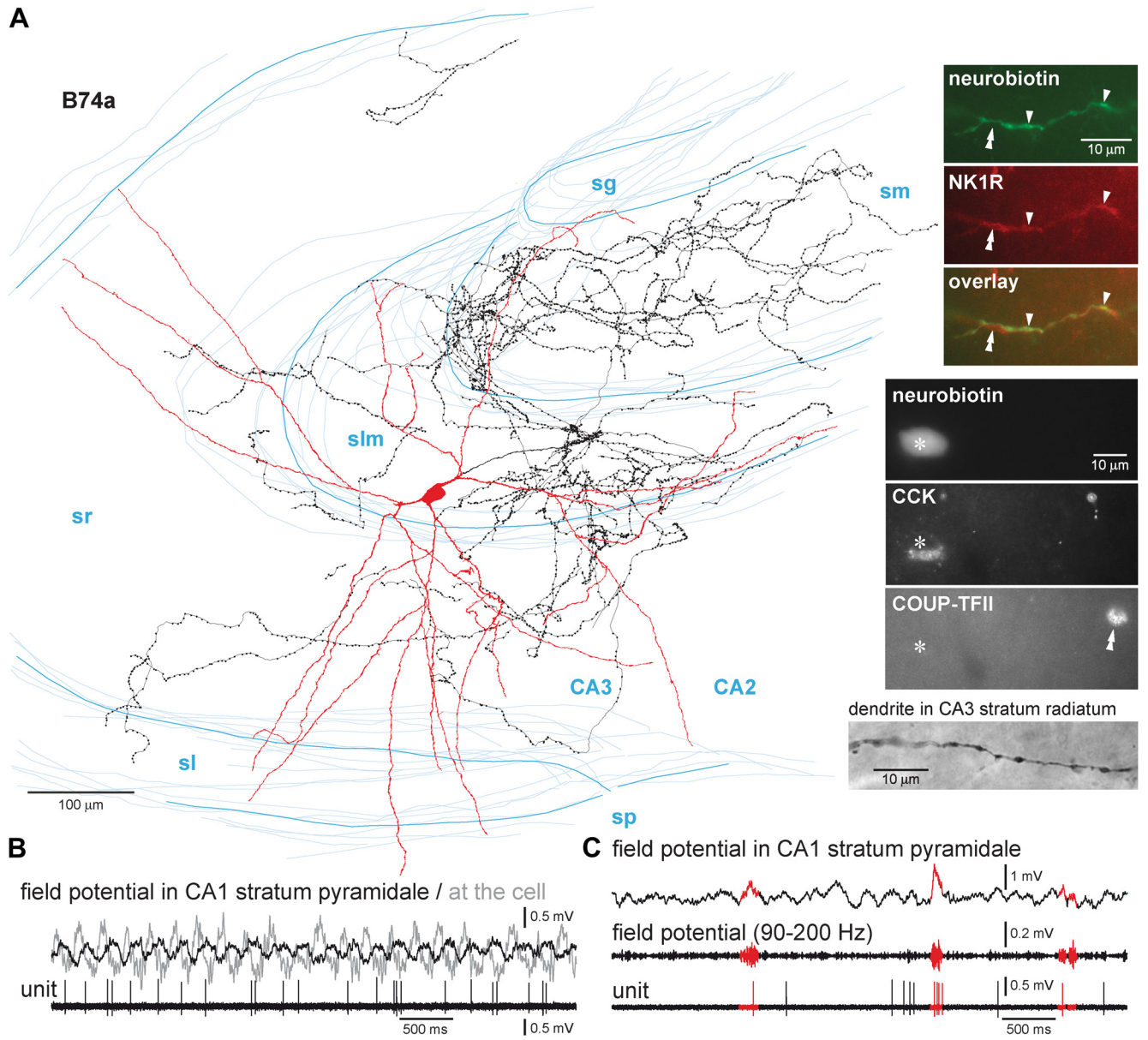

Figure 5. Visualization and firing patterns of a CCK-containing dendritic-layer-innervating cell. ***A***, Reconstruction (Neurolucida, three dimensional) of cell B74a, projected onto a plane approximately transverse to the hippocampus. This axis maximizes the overlap of layer boundaries recorded in individual coronal sections (thin blue lines); a best fit of "average" boundaries is shown by thick blue lines. The somato-dendritic domain is shown in full (red, 10 sections), the axon (black) only from four consecutive 70-μm-thick sections also including the soma. Top inset, Immunoreactivity of a dendrite of the cell (arrowheads, green) and another adjoining dendrite (double arrowheads) for the NK_1R (red, middle). Bottom inset, The soma of the cell (top, asterisk) is immunoreactive for CCK (middle) in the perinuclear Golgi apparatus but is immunonegative for the transcriptional regulator COUP-TFII (bottom). The double arrowhead points to an immunopositive nucleus of an adjacent cell. The image at the bottom shows a dendritic segment in the stratum radiatum (sr). ***B***, Theta-oscillation-associated firing patterns. Field potential traces recorded from glass electrodes in CA1 stratum pyramidale (top, black) and CA3 stratum lacunosum-moleculare (top, gray). With the latter electrode, we also recorded action potentials of the cell (bottom), which fired on the ascending phase of most CA1 theta cycles. The cell is phase coupled to theta oscillations recorded locally as well, which is phase shifted (~180°) but highly coherent with CA1 theta. ***C***, Sharp wave-associated firing pattern. Field potential recording from CA1 stratum pyramidale (top) with the sharp wave/ripple complexes plotted in red. Sharp waves are associated with increased oscillation amplitude in the ripple band (90–200 Hz, middle). The firing of the cell (bottom) is variable during sharp waves. sg, Stratum granulosum; slm, stratum lacunosum-moleculare; sm, stratum moleculare; sl, stratum lucidum; sp, stratum pyramidale.

←

(*Figure legend continued.*) theta oscillations shows rhythmic discharges preferentially occurring on the ascending phase and peak of theta cycles. ***D***, Sharp wave-associated firing pattern of the cell. The sharp waves (red, CA1) are associated with increases in the amplitude of 90–200 Hz oscillations (ripples; middle trace). The trace was expanded from the brain-state transition period (boxed in ***B***), in which the cell was still active and fired during some of the sharp waves (asterisks, see also Fig. 8). sg, Stratum granulosum; sm, stratum moleculare; slm, stratum lacunosum-moleculare; sp, stratum pyramidale; so, stratum oriens.

layer-innervating cells showed differential sharp wave responses, because both J45a and B74a significantly increased ($p < 0.05$, Mann–Whitney U test; Table 2) their firing rates when sharp waves occurred. However, not all sharp waves were associated with repetitive firing (Figs. 4*D*, 5*C*, 8; Table 2). Activation of cell J45a seemed to depend on the brain state: sharp waves that occurred in transition periods or close to theta periods were often associated with firing (Fig. 4*D*), but those nested into non-theta–non-sharp wave periods, when the cell was completely silenced anyway, did not result in firing

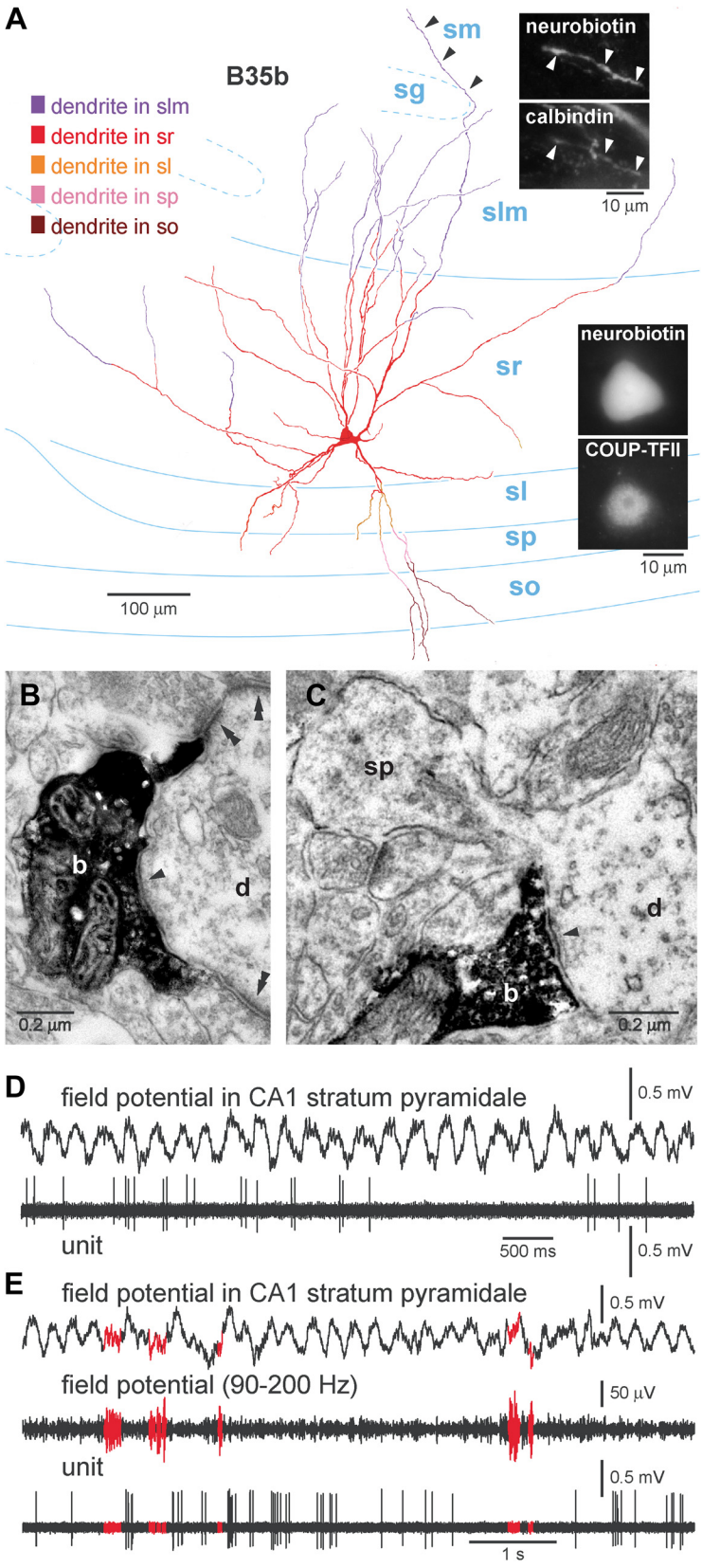

Figure 6. Visualization and firing patterns of a CA3 interneuron (B35b) coexpressing CCK, calbindin, and the COUP-TFII transcription factor. ***A***, Reconstruction showing the soma (red) located in the stratum radiatum (sr) and the dendrites in their full extent (15 consecutive 70-μm-thick sections) color coded to represent dendritic segments in different layers (see inset). Note the marked shift in layer positions in this two-dimensional projected view attributable to the curvature of the hippocampus; approximate layer boundaries around the soma are shown in blue. The approximate boundary of the dentate gyrus granule cell layer (sg) is projected onto the coronal plane (broken blue lines). The dendrites enter the stratum oriens (so) reaching the alveus, and one dendrite invades the dentate molecular layer (sm, black arrowheads). Top inset, A dendritic segment (arrowheads) is immunoreactive for calbindin. Bottom inset, Nucleus of the cell is immunopositive for the nuclear transcriptional regulator COUP-TFII. ***B***, ***C***, Electron micrographs showing boutons (b) of the labeled cell making type II synapses (arrowheads) onto a dendrite (d) of another interneuron receiving also type I synapses onto its shaft (***B***, double arrowheads) and onto a dendrite of a pyramidal cell (***C***) emitting also a dendritic spine (sp). ***D*** shows the theta-oscillation-associated firing pattern, with a field potential trace from the CA1 stratum pyramidale (top) and action potentials of the cell (bottom). The cell fires on the descending phase of some theta cycles. ***E***, Sharp wave/ripple (red)-associated firing pattern showing field potential recording (CA1, top) and its isolated 90–200 Hz component (middle) nested into theta oscillations. Action potential activity (bottom) appears to be suppressed during the sharp waves. slm, Stratum lacunosum-moleculare; sl, stratum lucidum; sp, stratum pyramidale.

(Fig. 4*B*). The activity of the calbindin-positive dendritic-layer-innervating cell J65a was suppressed during sharp wave/ripple complexes, as were the other two cells expressing calbindin (and COUP-TFII; $p \ll 0.01$ for J65a and B35b and $p = 0.04$ for J38b, Mann–Whitney U test; Figs. 6*E*, 8; Table 2*)*.

Recording gamma oscillations in anesthetized rats

Gamma oscillations occupy a large frequency range (in most studies 30–100 Hz) and show complex time–frequency dynamics (Colgin et al., 2009). To capture possible frequency-dependent variations of spike timing relative to gamma oscillations, we used wavelet-based "phase–frequency" plots that permit spectral analysis of relationship between field potential oscillation phase and spike timing. To include all potential frequency components compared with a previous study of CA1 interneurons (30–80 Hz; Tukker et al., 2007), we extended the spectral range of analysis to 15–100 Hz, and we consider oscillations between 25 and 100 Hz as belonging to the gamma range. Because several CCK-expressing interneurons virtually cease firing when the network is not in the theta state (Klausberger et al., 2005 and this study), we limited our analyses to theta periods.

In drug-free animals, hippocampal gamma oscillations are modulated by theta oscillations in a frequency-dependent manner that reveals different physiologically relevant bands of gamma oscillations (Bragin et al., 1995; Csicsvari et al., 2003; Colgin et al., 2009; Tort et al., 2009). To test for the presence of such organization in urethane-anesthetized animals, we analyzed how normalized gamma oscillation amplitude

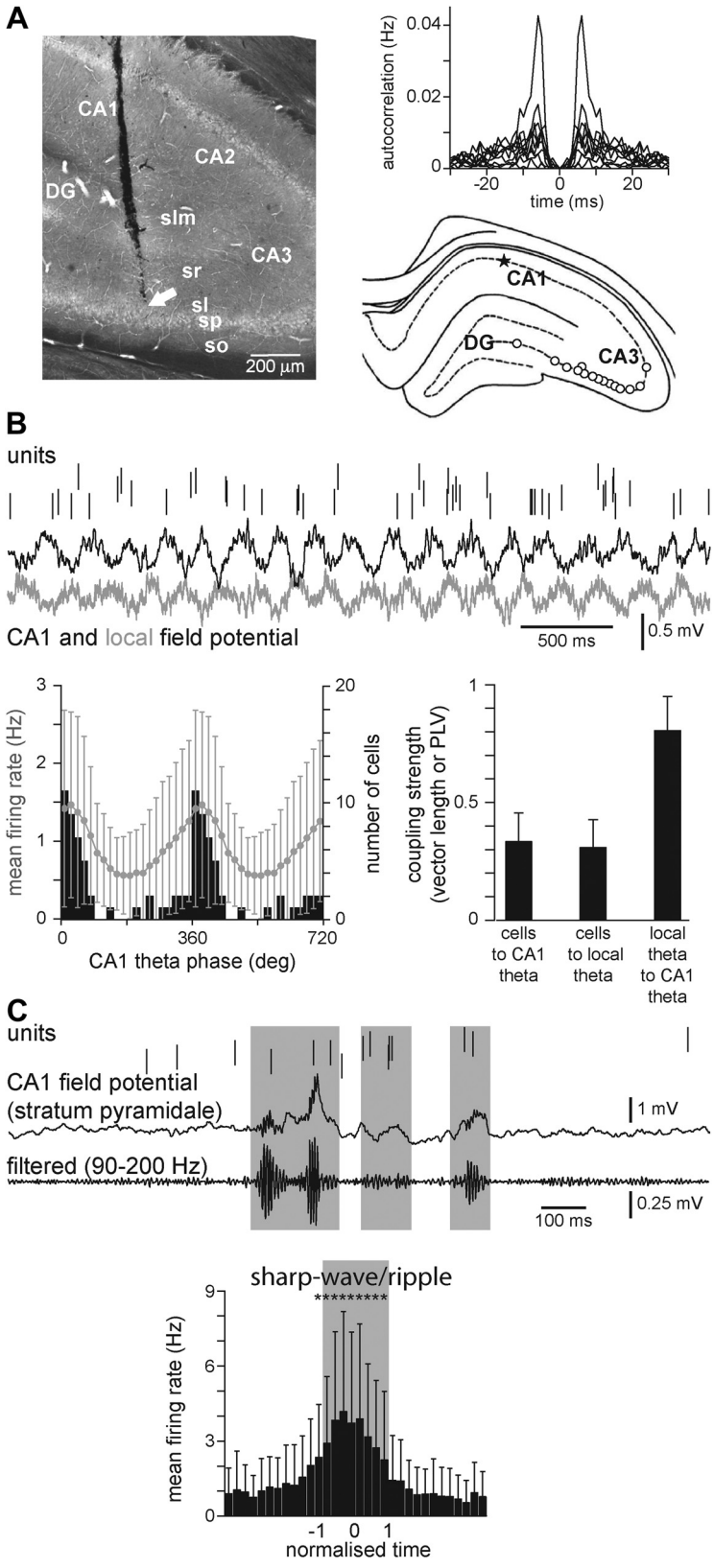

Figure 7. Theta oscillation and sharp wave/ripple-associated firing patterns of CA3 pyramidal cells. ***A***, Recording CA3 pyramidal cells with tetrodes. The track of a pair of tetrodes (left) is visualized by HRP reaction in a coronal section of the dorsal hippocampus. The tip of the track (arrow) is at the border between the stratum lucidum (sl) and the stratum pyramidale (sp) of CA3b. In this experiment (B52), 15 neuronal units were isolated from the two tetrodes, 10 of which were classified as putative pyramidal cells. The autocorrelograms of these 10 cells (top right) all have a peak at <10 ms. The autocorrelograms were multiplied by the firing rates of the cells after normalization; hence, the unit of the ordinate is hertz. The bottom right plot shows the approximate tetrode recording positions (open circles) and the CA1 glass electrode (star) mapped onto the outline of a section for all 15 experiments.

spectra in CA3 and CA1 areas depend on CA1 theta phase (Fig. 9*C*). In 13 of 15 tetrode recordings from CA3 stratum pyramidale (Fig. 9*C*) and five of six analyzed glass electrode recordings from the CA3 stratum radiatum, two separate bands of gamma oscillations were identified. Low-frequency gamma oscillations (25–45 Hz) were intense around the peak (140–280°) and suppressed around the trough of CA1 theta. High-frequency gamma oscillations (55–100 Hz) showed a complementary phase distribution and peaked around the trough of CA1 theta (260–70°; that is 260–430°). In the CA1 region ($n = 21$ glass electrode recordings in stratum pyramidale; data not shown), the bimodality of theta coupling of the oscillation amplitude across the gamma frequency range was less obvious. The low-frequency gamma component (25–55 Hz) occurred around the theta peak, whereas high-frequency gamma was not modulated by theta (10 of 21 experiments) or coupled to its ascending phase. This analysis discloses only coupling of gamma to theta oscillations but does not address the presence or significance of the power of oscillations in any particular gamma bands per se.

←

B, Theta-oscillation-associated firing. Top, Representative field potential recordings from the CA1 stratum pyramidale (black) and from the tetrode in CA3 stratum pyramidale (gray) along with the co-recorded putative pyramidal cell spike times (vertical ticks, individual units shifted vertically; experiment B52). Bottom, Data for all putative CA3 pyramidal cells. Left, Gray circles represent the firing rate averaged across all CA3 pyramidal cells ($n = 49$, 15 experiments; mean ± SD) as a function of the phase of theta oscillations in the CA1 stratum pyramidale (18° bins; 0°, 360°, and 720° mark the troughs; two theta cycles are shown). The distribution of mean firing phases of pyramidal cells significantly coupled to CA1 theta oscillations ($n = 46$ of 49 cells) is shown by black bars. Right, Average ± SD vector lengths for cells significantly coupled to theta oscillations in either CA1 (left bar; $n = 49$) or at the tetrode (middle bar, $n = 38$) and average ± SD theta PLV between the two field potentials (right bar; $n = 12$). ***C***, Firing of pyramidal cells associated with sharp wave/ripple complexes. Top, field potential recording (middle) of sharp wave/ripple complexes (gray background) from the CA1 stratum pyramidale and filtered trace (90–200 Hz; bottom) are shown below the spike times of concurrently recorded pyramidal cells (vertical ticks; experiment B52). Individual units are shifted. Bottom, Firing rate of all pyramidal cells ($n = 49$ units, 15 experiments). In each bin, the firing rate of all units was averaged and is shown as a function of time normalized to the occurrence of sharp waves in CA1 (gray background; −1, sharp wave starts; 1, sharp wave ends; 0, peak power in the 90–200 Hz range). The first and the last 12 bins (white background) represent the time before and after the sharp waves. Asterisks denote significance at $p < 0.05$ level (one-way ANOVA, followed by multiple comparisons with Bonferroni's correction). DG, Dentate gyrus; slm, stratum lacunosum-moleculare; sr, stratum radiatum; so, stratum oriens.

Table 1. Soma location, axonal, and dendritic distribution and neurochemical expression profiles of CCK-expressing CA3 interneurons

Different cell types are indicated by the same color code as in Figure 8. In the left half, the approximate axon and dendrite distribution is displayed. The density (relative to the whole arbor; nonquantitative) of processes in layers and sublayers is coded by shades of black (axon) and red (dendrite). Soma location is marked by a black dot. In the right half, the expression of different molecules, as determined by immunohistochemistry, is shown. Red, Immunopositive; green, immunonegative; nc, not conclusive; not decor, not decorated. The letters in parentheses denote the compartment that we tested for the presence of the molecule (s, soma; d, dendrite; a, axon) with occasional reference to the intensity of immunoreactivity (w, weak). DG, dentate gyrus; dist, distal (to pyramidal layer); gran, granule cell layer; lm, stratum lacunosum-moleculare; luc, stratum lucidum; mid, middle; mol, molecular layer; ori, stratum oriens; prox, proximal (to pyramidal layer); pyr, stratum pyramidale; rad, stratum radiatum.

Frequency-dependent phase coupling of CA3 pyramidal cells to gamma oscillations

Forty-six of 49 pyramidal cells (94%) showed significant ($p < 0.01$, Rayleigh's test of uniformity) phase coupling to at least one segment of the gamma frequency range oscillations recorded locally (Fig. 9*A*,*B*, top). For pyramidal cells, the strength of phase locking, measured as the mean vector length, showed marked frequency dependence (Fig. 9*A*,*B*). We have detected weak if any coupling below 30 Hz, a steep increase between 35 and 55 Hz, and a plateau extending to 100 Hz. Although coupling spanned both high- and low-gamma frequency ranges, no distinct peaks or obvious signs of bimodality were observed in the mean vector length spectra (Fig. 9*A*,*B*). The phase preference of CA3 pyramidal cells was consistent over the whole gamma frequency range (Fig. 9*B*), regardless of the exact location of the cells within the CA3 area (Fig. 7). The phase preference of pyramidal cells depended on gamma frequency and shifted from the trough (~350°) at the highest frequencies to early ascending phase (~60°) at 40 Hz. Coupling to CA1 gamma oscillation was also detected (25 of 49 cells, 51%), but phase locking was much weaker and limited to a narrower frequency range (~45–85 Hz; Fig. 9*A*, *B*).The distribution of mean phase spectra was consistent across cells (Fig. 9*B*). Oscillations were significantly phase coupled between CA1 and CA3 over the whole gamma range (shuffling analysis; $n = 35$; CA3 recordings from different layers), with PLV slightly higher for the low-frequency (~0.3) than for the high-frequency (~0.25; Fig. 9*D*; only tetrode recordings were analyzed in CA3) gamma band. The CA3–CA1 phase difference was consistent across experiments (Fig. 9*D*), shifting from ~80° at 90 Hz to ~170° at 35 Hz, which compares well with the phase relationships of CA3 pyramidal cells to CA3 and CA1 gamma oscillations (compare top and bottom plots in Fig. 9*B*,*D*).

Differential frequency-dependent phase coupling of CCK-expressing CA3 interneurons to gamma oscillations

Interneurons showed diversity in the frequency dependence of their phase coupling to local and CA1 gamma oscillations (for representative examples, see B34b and J45a in Fig. 10*A*). When referenced to local (CA3 stratum radiatum) oscillations, spikes of perforant-path-associated cell B34b showed a non-uniform distribution ($z > 4.6$, that is $p < 0.01$, Rayleigh's test) with a strong gamma phase-dependent accumulation of spikes from ~25 to 100 Hz (Fig. 10*A*, top left, *B*). In contrast, the firing of the dendritic-layer-innervating cell J45a was significantly ($z > 4.6$, that is $p < 0.01$, Rayleigh's test) phase coupled to gamma oscillations only above 55 Hz (Fig. 10*A*, top right). Comparison of phase-locking spectra across all interneurons (Fig. 10*C*,*D*) showed frequency-dependent coupling to local gamma oscillations that was correlated with the cell type (compare Fig. 10*C*,*D*, top plots, and Table 1). Perforant-path-associated cells having dendrites excluded from stratum lacunosum-moleculare (Fig. 3*A*; Table 1) were strongly phase coupled to gamma oscillations over a wide frequency range, (Fig. 10*C*,*D*, purple–pink). In contrast, dendritic-layer-

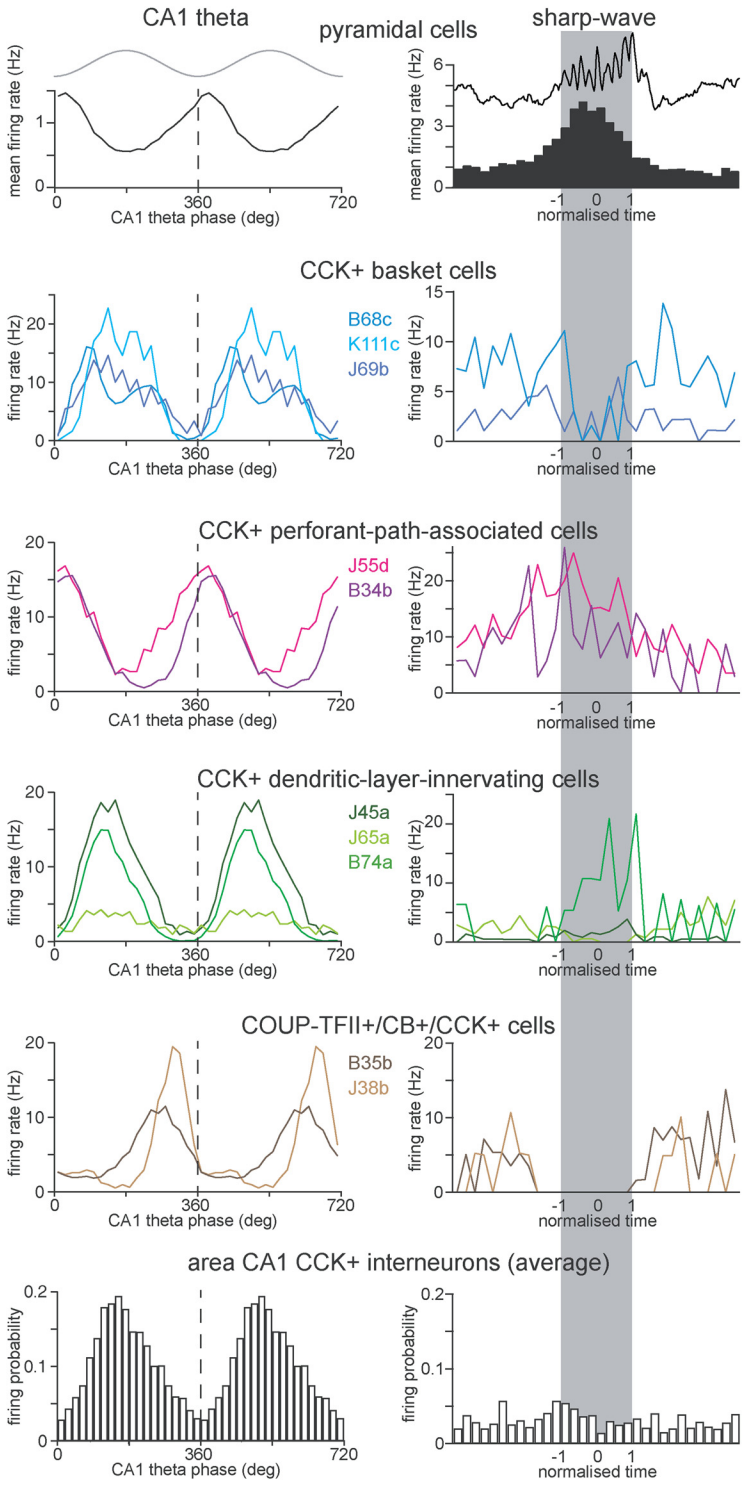

Figure 8. Theta oscillation and sharp wave/ripple-associated firing patterns of CA3 pyramidal cells and CCK-containing interneurons. Different cell types are indicated by the same color code as in Table 1. Mean firing rate of putative CA3 pyramidal neurons (top row, black, $n = 49$, as in Fig. 7) and firing rates of individual CA3 interneurons (rows 2–5) as a function of theta phase (top, gray) in the CA1 stratum pyramidale (left column; 18° bins; 0°, 360°, and 720° represent troughs, data duplicated to show two cycles). Sharp wave-associated firing is shown on the right (normalized time; 0, peak power in 90–200 Hz range). The vertical gray bar shows the duration of the sharp wave/ripple complex. Top, An example field potential recording from the CA1 stratum pyramidale. The interneurons are shown in four groups, as defined in Results; the color code of individual cells matches that of Table 1. In the bottom row, theta phase and sharp-wave-dependent fluctuations in average firing probability of nine CA1 CCK-expressing interneurons (data from Klausberger et al., 2005) are plotted for comparison. The average firing rate of CA1 area CCK-expressing interneurons was 8.8, 1.2, and 1.7 Hz during theta, non-theta–non-sharp wave, and sharp wave periods, respectively.

innervating cells and basket cells that extended their dendrites across strata lacunosum-moleculare and radiatum were phase coupled only to fast gamma oscillations (>50 Hz; Fig. 10*C*,*D*, blue and green). The cells coexpressing COUP-TFII and calbindin showed either strong (J38b) or weaker (B35b) coupling (Fig. 10*D*). Except for the cells showing strong phase coupling to CA3 slow gamma oscillations (B34b, J55d, and J38b), which showed phase coupling to slow gamma in CA1 as well, phase coupling to CA1 gamma oscillations was generally weak (Fig. 10*C*,*D*, bottom plots). Cell J45a showed no significant coupling to CA1 gamma (Fig. 10*A*, bottom right, *D*), and K111c was not included in this analysis because the CA1 electrode was located in stratum radiatum.

With reference to gamma oscillations in either the CA3 or CA1 areas, the phase preference spectra for interneurons showed frequency-dependent shifts to earlier phases with increasing frequencies (except for B35b and J38b; Fig. 10*C*) similar to those observed for pyramidal cells. Because gamma oscillations may display layer-dependent phase offsets that may become unpredictable in the curvature of the CA3 area, the actual phase preference data relative to local gamma oscillations should be interpreted with caution. Indeed, unlike the case of tetrode recordings, the phase offset spectra between the local CA3 and the reference CA1 electrodes showed a high variability (Fig. 10*E*, left). To predict the relative phase relationship of the firing of interneurons and pyramidal cells, we calculated the interneuron phase preference curves with reference to gamma oscillations in the stratum pyramidale of CA3 (Fig. 10*E*, right). For two cells (B34b and B35b), we could calculate the phase preference curves directly based on recordings from a tetrode located in CA3 stratum pyramidale (Fig. 10*E*, right, broken lines). These showed substantial overlap to the calculated phase preference spectra, corroborating the validity of the approach. A conservative conclusion drawn from the phase preference spectra, using local CA3 (Fig. 10*C*, top plot), CA1 (Fig. 10*C*, bottom plot), or calculated CA3 stratum pyramidale (Fig. 10*E*, right) gamma oscillation as a reference, is that CCK-expressing interneurons as a population fire with a 0° to +90° phase offset with respect to CA3 pyramidal cells as a population (compare Fig. 9*B* with 10*C*,*E*). Be-

Table 2. Parameters of cellular firing associated with theta oscillations and sharp wave/ripple complexes

	Firing rate (Hz)		Theta				Sharp wave/ripple		
Cell	Theta	Non-theta–non-sharp wave	Vector length[b]	Mean phase (°)[b]	Active cycles (%)	Spikes in cycles	n[f]	Rate (Hz) outside sharp wave	Rate (Hz) during sharp wave
Pyramidal (mean)	0.91 ± 0.68	0.72 ± 0.51	0.33 ± 0.12[c]	22 ± 50[d]	17 ± 12	1.34 ± 0.27	n.a.	0.83 ± 0.50[g]	3.8 ± 2.6[a,g]
Basket									
K111c	9.50	n.r.	0.56	165	95	2.54	4 (0)	n.e.d	n.e.d.
B68c	7.33	n.e.d.	0.32	133[e]	86	2.11	44 (15)	5.30	3.49
J69b	7.32	0.99[a]	0.32	147	90	2.23	93 (15)	2.17	2.33
Perforant-path-associated									
B34b	5.64	1.26[a]	0.56	38	81	2.04	42 (20)	1.67	9.78[a]
J55d	8.96	6.14[a]	0.35	15	91	2.54	168 (129)	6.73	17.88[a]
Dendritic-layer-innervating									
J45a	8.70	0.01[a]	0.50	143	97	2.35	225 (28)	0.82	1.83[a]
B74a	5.57	n.r.	0.63	134	83	1.63	16 (9)	1.92	9.92[a]
J65a	2.55	2.93	0.24	141	51	1.20	128 (4)	3.98	0.36[a]
COUP-TFII $^+$ and calbindin $^+$									
B35b	5.66	2.01[a]	0.42	261	67	2.11	51 (0)	4.32	0[a]
J38b	5.69	n.e.d.	0.61	302	79	1.80	22 (0)	2.55	0[a]

n.r., Not recorded; n.e.d., not enough data for statistical assessment; n.a., not applicable.

[a] $p < 0.05$, Mann–Whitney U test.

[b] Calculated to theta oscillations recorded from CA1 stratum pyramidale or equivalent.

[c] Mean ± SD, averaged across significantly coupled cells; $n = 46$.

[d] Circular mean angle ± circular SD, averaged across significantly coupled cells ; $n = 46$.

[e] Double peak at 117° and 243°. The spikes on the ascending and descending phases were not segregated into different theta cycles because the distribution of the mean phases calculated for individual theta cycles (taken from trough to the next trough) was unimodal.

[f] Number of sharp waves (active sharp waves).

[g] Mean ± SD, averaged across cells with significant change; $n = 40$.

cause the slope of the preferred phase versus frequency curves is similar for pyramidal cells and most interneurons, the phase difference (0°-90°) rather than the time difference (ranging from 10 to 4 ms between 25 and 100 Hz for a 90° phase difference) is constant across several frequencies.

Discussion

Specialization of CCK-expressing interneuron types

We have demonstrated the diversity of CCK-containing interneurons and defined several cell types. The specializations observed in dendritic and axonal distributions and in protein expression is mirrored by preferential firing on ascending, trough, or descending phases of theta oscillations recorded in anesthetized rats. All CCK-expressing interneurons phase lock to fast (50–100 Hz) gamma oscillations, but only cells lacking dendrites in the stratum lacunosum-moleculare are also coupled to slower (25–45 Hz) oscillations. On average, during sharp waves, the firing rate of CCK-expressing interneurons is suppressed (cells containing calbindin), remains unchanged (basket cells), or increases (other cells).

In area CA1, several types of CCK-expressing interneuron are similarly coupled to network oscillations *in vivo* (Klausberger et al., 2005; Tukker et al., 2007). Temporal segregation of spike timing of CCK-containing interneurons in the CA3 area supports cell-type-specific contributions to network operations (Fig. 8). Diversity of CCK-expressing interneurons is extensive; we have not encountered mossy-fiber-associated cells (Vida and Frotscher, 2000) or VIP coexpressing basket cells (Acsády et al., 1996b). Furthermore, some correlations, such as between calbindin content and sharp wave responses, extend over different cell types. Nevertheless, the intersections of interneurons defined by protein expression, dendritic and axonal distribution, and firing patterns leads to an explanation of interneuron diversity also in the CA3 area.

Analysis of postsynaptic targets of CCK-expressing interneurons in area CA1 showed that principal cells are the primary targets of these cells (Klausberger et al., 2005). Electron microscopic analysis of postsynaptic targets of unidentified basket cells (Gulyás et al., 1993; Acsády et al., 1996a,b) and of a cell similar to the CCK-expressing dendritic-layer-innervating cells reported here (Gulyás et al., 1993) suggests a similar postsynaptic target distribution in the CA3 area. Indeed, the small sample we took from one neuron showed that pyramidal cell dendrites were the main targets. Furthermore, the conspicuous coalignment of the axons of individual non-basket, CCK-expressing interneurons with the associational (strata oriens and radiatum) or the perforant path (stratum lacunosum-moleculare) glutamatergic inputs to pyramidal cells provides a structural basis for the pathway-specific presynaptic modulation of glutamate release via presynaptic $GABA_B$ receptors (Scanziani et al., 1992), abundant on many glutamatergic terminals (Kulik et al., 2003). Thus, the glutamatergic input pathway-specific dendritic inhibition could act simultaneously via fast postsynaptic $GABA_A$ receptors and slower presynaptic and postsynaptic $GABA_B$ receptors.

Pyramidal cell firing patterns in anesthetized rats

Most studies report pooled interneuronal behavior attributable to difficulties of identification without labeling (but see Csicsvari et al., 1999b; Czurkó et al., 2011). The urethane-anesthetized rat offers a useful alternative for the dissection of brain-state-dependent contributions of identified neurons to slow oscillations (Hahn et al., 2007), sharp wave/ripple complexes (Ylinen et al., 1995), atropine-sensitive theta oscillations (Kramis et al., 1975; Buzsáki, 2002), and gamma oscillations (Penttonen et al., 1998; Atallah and Scanziani, 2009), but our data will need confirmation by recording identified interneurons in drug-free animals. Similar to our observations, CA3 pyramidal cells in drug-free rats increase firing before and throughout sharp waves (Csicsvari et al., 1999a, 2000), and both CA3 and CA1 pyramidal cells fire most on the trough of theta oscillations (Fox et al., 1986; Buzsáki, 2002). More recently, Mizuseki et al. (2009) documented that dentate granule cells and CA3c pyramidal cells fire on the descending phase of theta cycles. Pyramidal cells in CA3c, however, receive no ento-

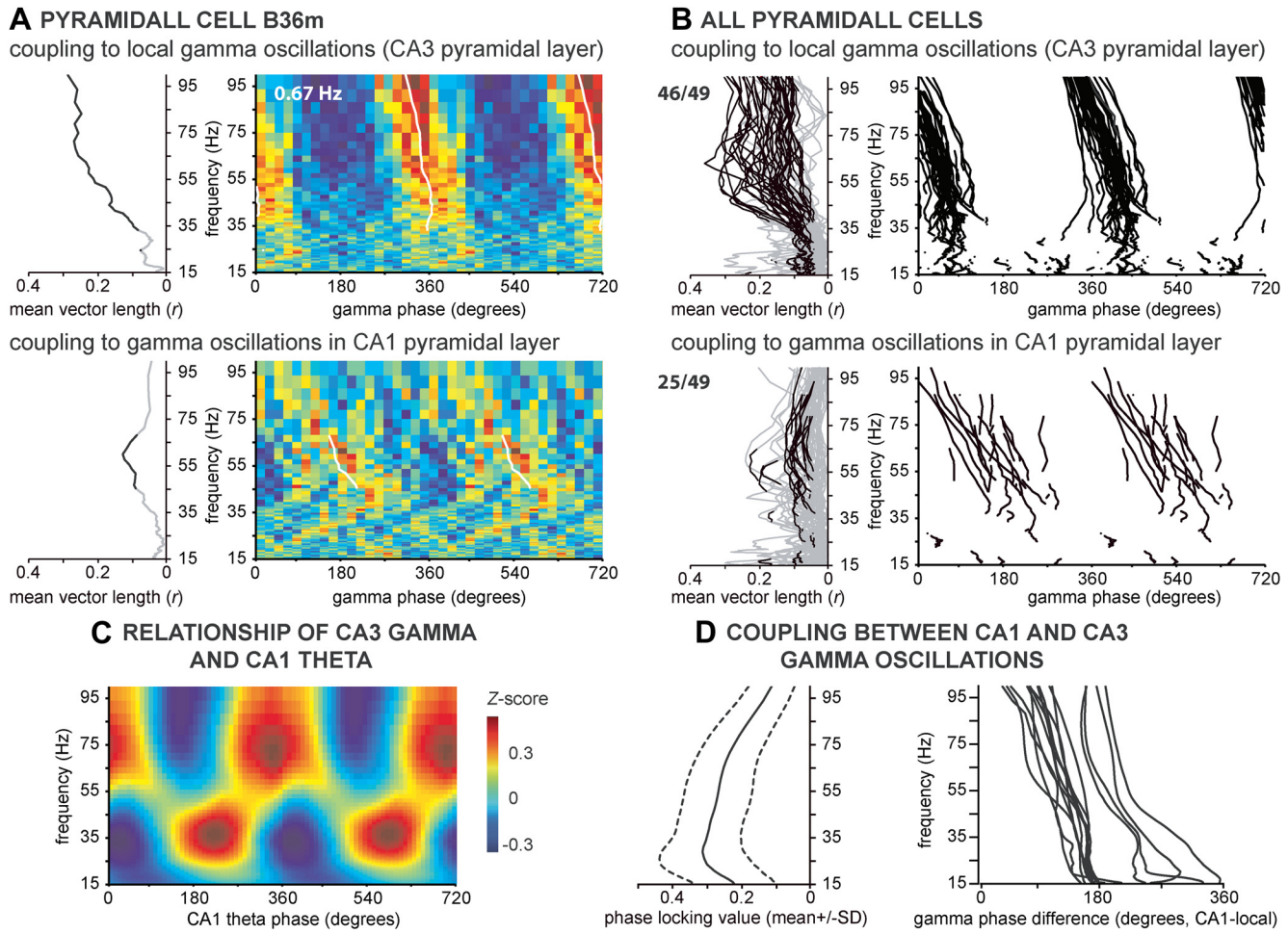

Figure 9. Phase coupling of spike timing of CA3 pyramidal neurons to gamma frequency oscillations during theta oscillations. ***A***, A representative putative pyramidal cell (B36m). Coupling of firing to the local (top; one tetrode wire, CA3) and the CA1 stratum pyramidale (bottom) field potential. Right, The numbers of spikes per bin are shown color coded as a function of gamma frequency and phase (0°, 360°, and 720°, troughs; cycles duplicated). The color code is normalized between the minimum (coldest) and the maximum (warmest) values of the plot. The mean phase with significant coupling is plotted as a white line. The mean firing rate during theta is shown in white. Left, The mean vector length for all frequencies provides a spectrum (gray) with the statistically significant values in black (Rayleigh's $z > 4.6$, $p < 0.01$). The firing of this cell was significantly coupled to 33.3–100 Hz (CA3) and 45.5–68.2 Hz (CA1) ranges. ***B***, Phase coupling of the CA3 pyramidal cell population to the local (top) and CA1 stratum pyramidale (bottom) oscillations. The mean vector length is plotted as a function of frequency (gray, left) with values for significantly non-uniform phase distributions (Rayleigh's $z > 4.6$, $p < 0.01$) plotted in black. Numbers (top left) refer to the proportion of cells with significant coupling in the 25–100 Hz range. The right panels show the significant values of the mean phase spectra. ***C***, Relationship of gamma oscillation amplitude and theta oscillation phase in a representative experiment. Two clear gamma frequency bands (25–45 and 55–100 Hz) can be distinguished by their preferential theta phase. The mean *Z*-score of instantaneous field potential gamma amplitude (wavelet modulus; color coded) in the CA3 stratum pyramidale as a function of gamma frequency and of the theta phase (CA1 stratum pyramidale; 0°, 360°, and 720°, troughs; cycles duplicated). The *Z*-transformation was done separately for each frequency, followed by averaging of the binned data over CA1 theta cycles. ***D***, Phase coupling between CA1 and CA3 strata pyramidale field potentials in the gamma frequency range. Left, PLV spectra averaged across all experiments [$n = 15$; mean (full line) ± SD (dashed line)]. Right, Phase difference spectra (CA1–CA3; 0° and 360°, in-phase; 180°, out-of-phase) of individual experiments. Note that the phase difference varies as a function of frequency.

rhinal input in stratum lacunosum-moleculare (Turner et al., 1995) and may fire differently from other CA3 pyramidal cells.

Specialization of CCK-expressing interneurons in spatial memory encoding and retrieval

The dendritic distributions of dendritic-layer-innervating and basket cells in strata lacunosum-moleculare and radiatum suggest that they integrate entorhinal and associational CA3 inputs. Lacking dendrites in stratum lacunosum-moleculare, perforant-path-associated cells have little direct entorhinal input and are probably driven by pyramidal cells. Computational models (Treves and Rolls, 1994) and experimental data (Kentros et al., 1998; Lee and Kesner, 2002; Nakazawa et al., 2002, 2003) suggest that, during encoding, entorhinal input patterns are associated with CA3 cell assemblies by strengthening connections onto coactive pyramidal cells. During memory retrieval, reexposure to incomplete perforant pathway representations reinstates cofiring of CA3 assemblies through strengthened associational collaterals (Treves and Rolls, 1992; Nakazawa et al., 2002; Fyhn et al., 2007). By sampling the input (perforant-path) and output (associational collaterals/commissurals) patterns of CA3, dendritic-layer-innervating interneurons may respond to sequences of entorhinal retrieval cues and learned CA3 associations. Indeed, CB_1R-expressing interneurons efficiently integrate inputs over 5–10 ms (Glickfeld and Scanziani, 2006), long enough for memory retrieval (de Almeida et al., 2007). Dendritic-layer-innervating interneurons and basket cells fire maximally on the late ascending phase of theta, when place cell assemblies fire first on a traversal (Skaggs et al., 1996; Dragoi and Buzsáki, 2006; Huxter et al., 2008). The resulting asynchronous, cannabinoid-sensitive inhibition persists for most of the forthcoming theta cycle (Hefft and Jonas, 2005; Daw et al., 2009) when, because of phase precession, pyramidal cell assembly sequences from earlier theta cycles are repeated (Skaggs et al., 1996; Dragoi and Buzsáki, 2006; Huxter et al., 2008). Release of GABA onto these repeatedly active pyramidal cells is selectively sup-

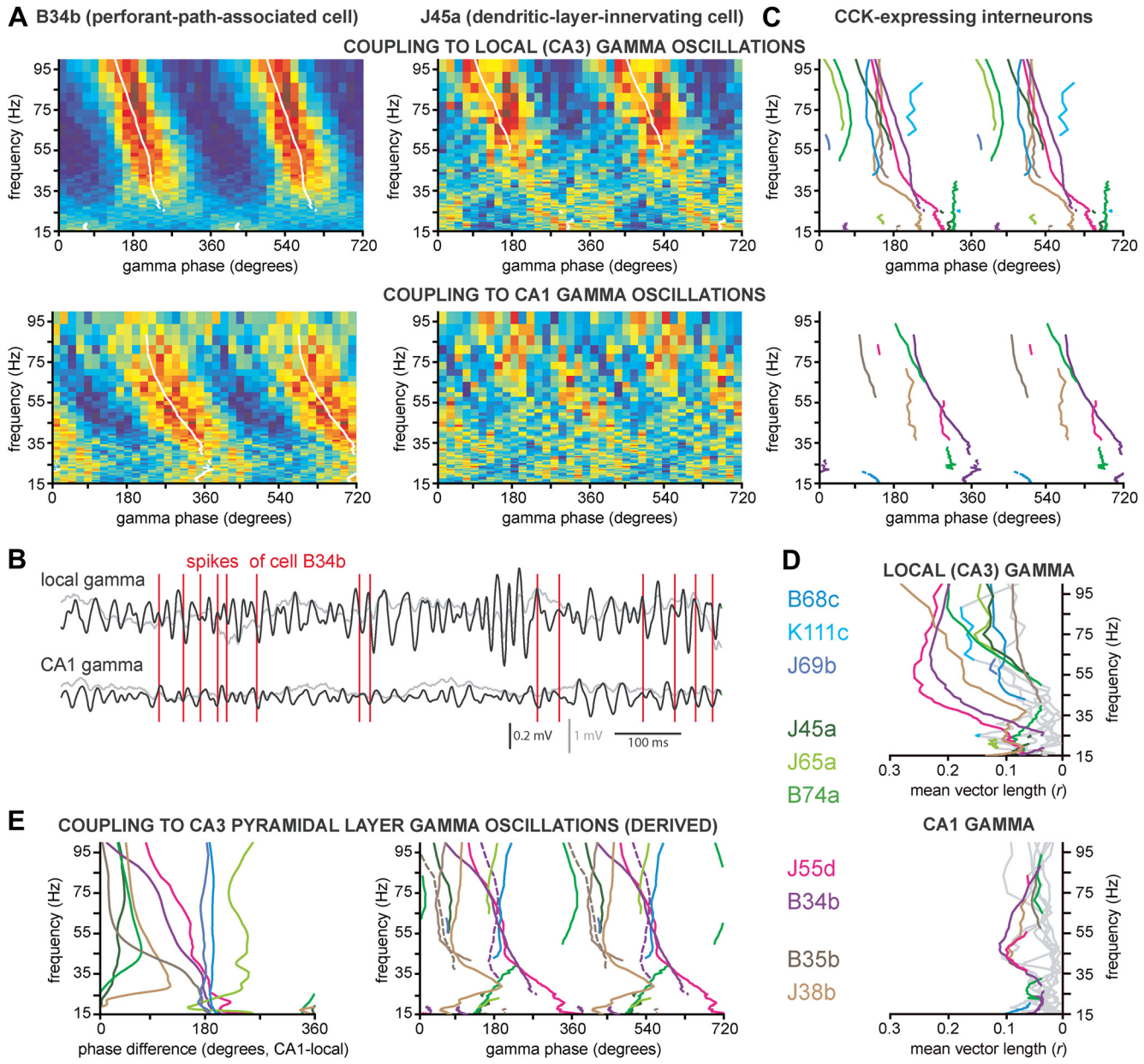

Figure 10. Phase coupling of spike timing in CCK-immunoreactive interneurons to gamma oscillations during theta oscillations. ***A***, Coupling to gamma oscillations (local, top row; CA1 stratum pyramidale, bottom row) in two representative interneurons, a perforant-path-associated cell (B34b, left) and a dendritic-layer-innervating cell (J45a, right; see Fig. 4), both located at the stratum radiatum and stratum lacunosum-moleculare border. The numbers of spikes per bin is color coded as a function of frequency and gamma phase (0°, 360°, and 720° are the troughs; cycles duplicated). The color code is normalized between the minima (coldest) and maxima (warmest) of the plots. The mean phase for frequencies with non-uniform (Rayleigh's $z > 4.6$, $p < 0.01$) phase distribution is plotted as a white line. In CA3, cell B34b was strongly coupled to the whole gamma range (25–100 Hz), whereas J45a was coupled only to fast (>55 Hz) gamma oscillations. ***B***, Recording traces showing phase coupling of spike timing in B34b (red lines) to local field potential (top traces) and field potential recorded from the CA1 (bottom traces). Field potential recordings before and after (25–100 Hz, bandpass) filtering are displayed in gray and black, respectively. Note that coupling to the slower frequencies is more apparent because of the higher amplitude of slower gamma cycles. Spikes of B34b preferentially occur on early descending phase of local and on late descending phase of CA1 gamma cycles (compare left plots in ***A***). ***C***, ***D***, Phase coupling of CCK-expressing interneurons to gamma frequency field potential oscillations in CA3 dependent on the laminar location of the cell (top) and in CA1 stratum pyramidale (bottom). ***C***, Significant values of the mean phase spectra. The color code is the same as in Figure 8 and Table 1. ***D***, The mean vector length at frequencies with uniform (gray) and non-uniform (color coded; Rayleigh's $z > 4.6$, $p < 0.01$) phase distributions. ***E***, Phase coupling between field potentials in CA1 stratum pyramidale and CA3 (local; color coded; K111 not plotted) in the gamma frequency range (left). To compare the phase spectra of CA3 interneurons with those of CA3 pyramidal cells (Fig. 9), we calculated the derived CA3 stratum pyramidale phase spectra for the interneurons (right) by first subtracting the coupling spectra between CA1 and local electrode (left plot) and then adding to the resulting derived CA1 phase spectra a representative coupling spectrum between CA1 and CA3 stratum pyramidale (the same for all cells, see Fig. 9). For two interneurons (B34b, B35b), we co-recorded the actual CA3 stratum pyramidale local field potential with a tetrode pair. These two nonderived CA3 stratum pyramidale coupling spectra are plotted with broken lines.

pressed by CB_1R-dependent DSI (Pitler and Alger, 1992; Hájos et al., 2000; Wilson and Nicoll, 2001), and this way inhibition may increase contrast between active and inactive cell assemblies (Freund et al., 2003; Klausberger et al., 2005). Indeed, exogenously applied cannabinoids compromise phase precession and erode temporal coordination of cell assemblies (Robbe et al., 2006; Robbe and Buzsáki, 2009). Interestingly, the activity of unidentified interneurons was selectively suppressed by exposure to novel environments (Wilson and McNaughton, 1993; Nitz and McNaughton, 2004). We speculate that the CCK-expressing dendritic-layer-innervating cells may

be among those cells because they require a coordinated entorhinal and associational input to discharge, which may not be established during the initial navigation through a novel environment. Through equalizing inhibition to individual principal cells, the lack of dendritic-layer-innervating cell activity could facilitate synaptic plasticity in the dentate gyrus (pattern separation; O'Reilly and McClelland, 1994; Leutgeb et al., 2007; McHugh et al., 2007) and CA3 stratum radiatum (associative coding; Treves and Rolls, 1994; Kentros et al., 1998; Nakashiba et al., 2008) and is thus conducive to the encoding of novel associations with new cell assemblies.

The dendritic fields of perforant-path-associated cells within the axonal termination of CA3 pyramidal cells explains their firing on the theta trough, coincident with maximum cofiring between established CA3 pyramidal cell assemblies and their entorhinal inputs (Hafting et al., 2008; Mizuseki et al., 2009; Quilichini et al., 2010). They support entorhino-hippocampal synaptic interactions and plasticity by providing endocannabinoid-sensitive feedback inhibition aligned to the entorhinal input on a theta phase crucial for plasticity.

CCK-expressing interneurons and gamma frequency coordination

The slow temporal dynamics of input (Glickfeld and Scanziani, 2006) and output (Hefft and Jonas, 2005) synapses of CCK-expressing interneurons may explain why parvalbumin-expressing, but not CB_1R-expressing, interneurons are thought to be instrumental in generating gamma oscillations *in vitro* (Mann et al., 2005; Gulyás et al., 2010) and *in vivo* (Fuchs et al., 2007; Tukker et al., 2007; Cardin et al., 2009). The weak gamma phase coupling of spike timing in dendritic-layer-innervating cells and basket cells supports this, and, although perforant-path-associated cells are strongly phase coupled to both slow and fast gamma oscillations, the distal position of their output synapses makes their direct involvement in field gamma oscillation generation in the somatic and apical dendritic layers unlikely. Instead, we suggest that they may entrain to gamma oscillations the efficacy of entorhinal input through the rhythmic dendritic IPSCs they generate in stratum lacunosum-moleculare. Their dynamic coupling is inherited from CA3 pyramidal cells, also phase coupled to a wide frequency range. Pyramidal cells can be entrained to entorhinal fast gamma oscillations or can engage in generating a slower CA3-initiated endogenous gamma rhythm (Bragin et al., 1995; Chrobak and Buzsáki, 1998; Csicsvari et al., 2003), which is then fed back to the entorhinal input zone of distal dendrites by CCK-expressing perforant-path-associated cells.

Diversity of protein expression in CCK-containing CA3 interneurons

The differential theta phase preference of interneurons expressing CCK, calbindin, and COUP-TFII is surprising. In strata radiatum and lacunosum-moleculare, most calbindin-expressing interneurons contain COUP-TFII (Fuentealba et al., 2010) and/or CCK (Cope et al., 2002; Somogyi et al., 2004). These cells are selectively targeted by serotonin- and VGLUT3-containing median raphe fibers that mediate theta-modulated fast glutamatergic and serotonergic activation (Morales and Bloom, 1997; Varga et al., 2009). Calbindin-expressing interneurons in CA1 stratum radiatum are also selectively targeted by a subset of VIP-expressing interneurons (Acsády et al., 1996a), which may inhibit them during sharp waves, observed here in the CA3.

In response to brain-state transitions, CCK-expressing interneurons show tonic firing rate changes (Klausberger et al., 2005). Nonsynaptically located receptors, such as mGluR1α and NK_1R (Liu et al., 1994; Acsády et al., 1997), may contribute to slow changes in cellular excitability, whereas the resulting release of neuropeptides may mediate some aspects of network-state transitions. The octapeptide CCK itself may thus contribute to a switch between slow-wave and theta states by facilitating glutamatergic transmission at all stages of hippocampal processing and regulating the balance between complementary inhibitory networks (Földy et al., 2007).

References

Acsády L, Görcs TJ, Freund TF (1996a) Different populations of vasoactive intestinal polypeptide-immunoreactive interneurons are specialized to control pyramidal cells or interneurons in the hippocampus. Neuroscience 73:317–334.

Acsády L, Arabadzisz D, Freund TF (1996b) Correlated morphological and neurochemical features identify different subsets of vasoactive intestinal polypeptide-immunoreactive interneurons in rat hippocampus. Neuroscience 73:299–315.

Acsády L, Katona I, Gulyás AI, Shigemoto R, Freund TF (1997) Immunostaining for substance P receptor labels GABAergic cells with distinct termination patterns in the hippocampus. J Comp Neurol 378:320–336.

Atallah BV, Scanziani M (2009) Instantaneous modulation of gamma oscillation frequency by balancing excitation with inhibition. Neuron 62:566–577.

Baude A, Nusser Z, Roberts JD, Mulvihill E, McIlhinney RA, Somogyi P (1993) The metabotropic glutamate receptor (mGluR1a) is concentrated at perisynaptic membrane of neuronal subpopulations as detected by immunogold reaction. Neuron 11:771–787.

Berens P (2009) CircStat: a Matlab toolbox for circular statistics. J Stat Software 31:21.

Bodor AL, Katona I, Nyíri G, Mackie K, Ledent C, Hájos N, Freund TF (2005) Endocannabinoid signaling in rat somatosensory cortex: laminar differences and involvement of specific interneuron types. J Neurosci 25:6845–6856.

Bragin A, Jandó G, Nádasdy Z, Hetke J, Wise K, Buzsáki G (1995) Gamma (40–100 Hz) oscillation in the hippocampus of the behaving rat. J Neurosci 15:47–60.

Brun VH, Otnass MK, Molden S, Steffenach HA, Witter MP, Moser MB, Moser EI (2002) Place cells and place recognition maintained by direct entorhinal-hippocampal circuitry. Science 296:2243–2246.

Buzsáki G (2002) Theta oscillations in the hippocampus. Neuron 33:325–340.

Buzsáki G, Czopf J, Kondákor I, Kellényi L (1986) Laminar distribution of hippocampal rhythmic slow activity (RSA) in the behaving rat: current-source density analysis, effects of urethane and atropine. Brain Res 365:125–137.

Cardin JA, Carlén M, Meletis K, Knoblich U, Zhang F, Deisseroth K, Tsai LH, Moore CI (2009) Driving fast-spiking cells induces gamma rhythm and controls sensory responses. Nature 459:663–667.

Chrobak JJ, Buzsáki G (1998) Gamma oscillations in the entorhinal cortex of the freely behaving rat. J Neurosci 18:388–398.

Cobb SR, Buhl EH, Halasy K, Paulsen O, Somogyi P (1995) Synchronization of neuronal activity in hippocampus by individual GABAergic interneurons. Nature 378:75–78.

Colgin LL, Denninger T, Fyhn M, Hafting T, Bonnevie T, Jensen O, Moser MB, Moser EI (2009) Frequency of gamma oscillations routes flow of information in the hippocampus. Nature 462:353–357.

Cope DW, Maccaferri G, Márton LF, Roberts JD, Cobden PM, Somogyi P (2002) Cholecystokinin-immunopositive basket and Schaffer collateral-associated interneurones target different domains of pyramidal cells in the CA1 area of the rat hippocampus. Neuroscience 109:63–80.

Csicsvari J, Hirase H, Czurko A, Buzsáki G (1998) Reliability and state dependence of pyramidal cell-interneuron synapses in the hippocampus: an ensemble approach in the behaving rat. Neuron 21:179–189.

Csicsvari J, Hirase H, Czurkó A, Mamiya A, Buzsáki G (1999a) Fast network oscillations in the hippocampal CA1 region of the behaving rat. J Neurosci 19:RC20(1–4).

Csicsvari J, Hirase H, Czurkó A, Mamiya A, Buzsáki G (1999b) Oscillatory coupling of hippocampal pyramidal cells and interneurons in the behaving rat. J Neurosci 19:274–287.

Csicsvari J, Hirase H, Mamiya A, Buzsáki G (2000) Ensemble patterns of hippocampal CA3-CA1 neurons during sharp wave-associated population events. Neuron 28:585–594.

Csicsvari J, Jamieson B, Wise KD, Buzsáki G (2003) Mechanisms of gamma oscillations in the hippocampus of the behaving rat. Neuron 37:311–322.
Czurkó A, Huxter J, Li Y, Hangya B, Muller RU (2011) Theta phase classification of interneurons in the hippocampal formation of freely moving rats. J Neurosci 31:2938–2947.
Daw MI, Tricoire L, Erdelyi F, Szabo G, McBain CJ (2009) Asynchronous transmitter release from cholecystokinin-containing inhibitory interneurons is widespread and target-cell independent. J Neurosci 29:11112–11122.
de Almeida L, Idiart M, Lisman JE (2007) Memory retrieval time and memory capacity of the CA3 network: role of gamma frequency oscillations. Learn Mem 14:795–806.
Dragoi G, Buzsáki G (2006) Temporal encoding of place sequences by hippocampal cell assemblies. Neuron 50:145–157.
Dupret D, O'Neill J, Pleydell-Bouverie B, Csicsvari J (2010) The reorganization and reactivation of hippocampal maps predict spatial memory performance. Nat Neurosci 13:995–1002.
Ferraguti F, Cobden P, Pollard M, Cope D, Shigemoto R, Watanabe M, Somogyi P (2004) Immunolocalization of metabotropic glutamate receptor 1α (mGluR1α) in distinct classes of interneuron in the CA1 region of the rat hippocampus. Hippocampus 14:193–215.
Földy C, Lee SY, Szabadics J, Neu A, Soltesz I (2007) Cell type-specific gating of perisomatic inhibition by cholecystokinin. Nat Neurosci 10:1128–1130.
Fox SE, Wolfson S, Ranck JB Jr (1986) Hippocampal theta rhythm and the firing of neurons in walking and urethane anesthetized rats. Exp Brain Res 62:495–508.
Freund TF, Antal M (1988) GABA-containing neurons in the septum control inhibitory interneurons in the hippocampus. Nature 336:170–173.
Freund TF, Buzsáki G (1996) Interneurons of the hippocampus. Hippocampus 6:347–470.
Freund TF, Katona I, Piomelli D (2003) Role of endogenous cannabinoids in synaptic signaling. Physiol Rev 83:1017–1066.
Fuchs EC, Zivkovic AR, Cunningham MO, Middleton S, Lebeau FE, Bannerman DM, Rozov A, Whittington MA, Traub RD, Rawlins JN, Monyer H (2007) Recruitment of parvalbumin-positive interneurons determines hippocampal function and associated behavior. Neuron 53:591–604.
Fuentealba P, Klausberger T, Karayannis T, Suen WY, Huck J, Tomioka R, Rockland K, Capogna M, Studer M, Morales M, Somogyi P (2010) Expression of COUP-TFII nuclear receptor in restricted GABAergic neuronal populations in the adult rat hippocampus. J Neurosci 30:1595–1609.
Fyhn M, Molden S, Witter MP, Moser EI, Moser MB (2004) Spatial representation in the entorhinal cortex. Science 305:1258–1264.
Fyhn M, Hafting T, Treves A, Moser MB, Moser EI (2007) Hippocampal remapping and grid realignment in entorhinal cortex. Nature 446:190–194.
Glickfeld LL, Scanziani M (2006) Distinct timing in the activity of cannabinoid-sensitive and cannabinoid-insensitive basket cells. Nat Neurosci 9:807–815.
Gloveli T, Dugladze T, Rotstein HG, Traub RD, Monyer H, Heinemann U, Whittington MA, Kopell NJ (2005) Orthogonal arrangement of rhythm-generating microcircuits in the hippocampus. Proc Natl Acad Sci U S A 102:13295–13300.
Gulyás AI, Miles R, Hájos N, Freund TF (1993) Precision and variability in postsynaptic target selection of inhibitory cells in the hippocampal CA3 region. Eur J Neurosci 5:1729–1751.
Gulyás AI, Szabó GG, Ulbert I, Holderith N, Monyer H, Erdélyi F, Szabó G, Freund TF, Hájos N (2010) Parvalbumin-containing fast-spiking basket cells generate the field potential oscillations induced by cholinergic receptor activation in the hippocampus. J Neurosci 30:15134–15145.
Hafting T, Fyhn M, Bonnevie T, Moser MB, Moser EI (2008) Hippocampus-independent phase precession in entorhinal grid cells. Nature 453:1248–1252.
Hahn TT, Sakmann B, Mehta MR (2007) Differential responses of hippocampal subfields to cortical up-down states. Proc Natl Acad Sci U S A 104:5169–5174.
Hájos N, Katona I, Naiem SS, MacKie K, Ledent C, Mody I, Freund TF (2000) Cannabinoids inhibit hippocampal GABAergic transmission and network oscillations. Eur J Neurosci 12:3239–3249.
Hampson RE, Deadwyler SA (2000) Cannabinoids reveal the necessity of hippocampal neural encoding for short-term memory in rats. J Neurosci 20:8932–8942.
Harris KD, Henze DA, Csicsvari J, Hirase H, Buzsáki G (2000) Accuracy of tetrode spike separation as determined by simultaneous intracellular and extracellular measurements. J Neurophysiol 84:401–414.
Harris KM, Marshall PE, Landis DM (1985) Ultrastructural study of cholecystokinin-immunoreactive cells and processes in area CA1 of the rat hippocampus. J Comp Neurol 233:147–158.
Hartwich K, Pollak T, Klausberger T (2009) Distinct firing patterns of identified basket and dendrite-targeting interneurons in the prefrontal cortex during hippocampal theta and local spindle oscillations. J Neurosci 29:9563–9574.
Hazan L, Zugaro M, Buzsáki G (2006) Klusters, NeuroScope, NDManager: a free software suite for neurophysiological data processing and visualization. J Neurosci Methods 155:207–216.
Hefft S, Jonas P (2005) Asynchronous GABA release generates long-lasting inhibition at a hippocampal interneuron-principal neuron synapse. Nat Neurosci 8:1319–1328.
Henze DA, Borhegyi Z, Csicsvari J, Mamiya A, Harris KD, Buzsáki G (2000) Intracellular features predicted by extracellular recordings in the hippocampus in vivo. J Neurophysiol 84:390–400.
Huxter JR, Senior TJ, Allen K, Csicsvari J (2008) Theta phase-specific codes for two dimensional position, trajectory and heading in the hippocampus. Nat Neurosci 11:587–594.
Ilan AB, Smith ME, Gevins A (2004) Effects of marijuana on neurophysiological signals of working and episodic memory. Psychopharmacology (Berl) 176:214–222.
Isomura Y, Sirota A, Ozen S, Montgomery S, Mizuseki K, Henze DA, Buzsáki G (2006) Integration and segregation of activity in entorhinal-hippocampal subregions by neocortical slow oscillations. Neuron 52:871–882.
Jinno S, Klausberger T, Marton LF, Dalezios Y, Roberts JD, Fuentealba P, Bushong EA, Henze D, Buzsáki G, Somogyi P (2007) Neuronal diversity in GABAergic long-range projections from the hippocampus. J Neurosci 27:8790–8804.
Kamondi A, Acsády L, Wang XJ, Buzsáki G (1998) Theta oscillations in somata and dendrites of hippocampal pyramidal cells in vivo: activity-dependent phase-precession of action potentials. Hippocampus 8:244–261.
Katona I, Sperlágh B, Sík A, Käfalvi A, Vizi ES, Mackie K, Freund TF (1999) Presynaptically located CB1 cannabinoid receptors regulate GABA release from axon terminals of specific hippocampal interneurons. J Neurosci 19:4544–4558.
Kentros C, Hargreaves E, Hawkins RD, Kandel ER, Shapiro M, Muller RV (1998) Abolition of long-term stability of new hippocampal place cell maps by NMDA receptor blockade. Science 280:2121–2126.
Klausberger T, Magill PJ, Márton LF, Roberts JD, Cobden PM, Buzsáki G, Somogyi P (2003) Brain-state- and cell-type-specific firing of hippocampal interneurons in vivo. Nature 421:844–848.
Klausberger T, Marton LF, O'Neill J, Huck JH, Dalezios Y, Fuentealba P, Suen WY, Papp E, Kaneko T, Watanabe M, Csicsvari J, Somogyi P (2005) Complementary roles of cholecystokinin- and parvalbumin-expressing GABAergic neurons in hippocampal network oscillations. J Neurosci 25:9782–9793.
Kramis R, Vanderwolf CH, Bland BH (1975) Two types of hippocampal rhythmical slow activity in both the rabbit and the rat: relations to behavior and effects of atropine, diethyl ether, urethane, and pentobarbital. Exp Neurol 49:58–85.
Kulik A, Vida I, Luján R, Haas CA, López-Bendito G, Shigemoto R, Frotscher M (2003) Subcellular localization of metabotropic $GABA_B$ receptor subunits $GABA_{B1a/b}$ and $GABA_{B2}$ in the rat hippocampus. J Neurosci 23:11026–11035.
Lachaux JP, Rodriguez E, Martinerie J, Varela FJ (1999) Measuring phase synchrony in brain signals. Hum Brain Mapp 8:194–208.
Le Van Quyen M, Foucher J, Lachaux J, Rodriguez E, Lutz A, Martinerie J, Varela FJ (2001) Comparison of Hilbert transform and wavelet methods for the analysis of neuronal synchrony. J Neurosci Methods 111:83–98.
Lee I, Kesner RP (2002) Differential contribution of NMDA receptors in hippocampal subregions to spatial working memory. Nat Neurosci 5:162–168.
Leutgeb JK, Leutgeb S, Moser MB, Moser EI (2007) Pattern separation in the dentate gyrus and CA3 of the hippocampus. Science 315:961–966.
Leutgeb S, Leutgeb JK, Treves A, Moser MB, Moser EI (2004) Distinct ensemble codes in hippocampal areas CA3 and CA1. Science 305:1295–1298.
Lichtman AH, Dimen KR, Martin BR (1995) Systemic or intrahippocampal cannabinoid administration impairs spatial memory in rats. Psychopharmacology (Berl) 119:282–290.
Liu H, Brown JL, Jasmin L, Maggio JE, Vigna SR, Mantyh PW, Basbaum AI (1994) Synaptic relationship between substance P and the substance P receptor: light and electron microscopic characterization of the mismatch between neuropeptides and their receptors. Proc Natl Acad Sci U S A 91:1009–1013.

Lubenov EV, Siapas AG (2009) Hippocampal theta oscillations are travelling waves. Nature 459:534–539.
Mann EO, Suckling JM, Hajos N, Greenfield SA, Paulsen O (2005) Perisomatic feedback inhibition underlies cholinergically induced fast network oscillations in the rat hippocampus in vitro. Neuron 45:105–117.
McBain CJ, DiChiara TJ, Kauer JA (1994) Activation of metabotropic glutamate receptors differentially affects two classes of hippocampal interneurons and potentiates excitatory synaptic transmission. J Neurosci 14:4433–4445.
McHugh TJ, Jones MW, Quinn JJ, Balthasar N, Coppari R, Elmquist JK, Lowell BB, Fanselow MS, Wilson MA, Tonegawa S (2007) Dentate gyrus NMDA receptors mediate rapid pattern separation in the hippocampal network. Science 317:94–99.
McNaughton BL, Battaglia FP, Jensen O, Moser EI, Moser MB (2006) Path integration and the neural basis of the "cognitive map." Nat Rev Neurosci 7:663–678.
Mizuseki K, Sirota A, Pastalkova E, Buzsáki G (2009) Theta oscillations provide temporal windows for local circuit computation in the entorhinal-hippocampal loop. Neuron 64:267–280.
Montana V, Ni Y, Sunjara V, Hua X, Parpura V (2004) Vesicular glutamate transporter-dependent glutamate release from astrocytes. J Neurosci 24:2633–2642.
Montgomery SM, Buzsáki G (2007) Gamma oscillations dynamically couple hippocampal CA3 and CA1 regions during memory task performance. Proc Natl Acad Sci U S A 104:14495–14500.
Morales M, Bloom FE (1997) The 5-HT3 receptor is present in different subpopulations of GABAergic neurons in the rat telencephalon. J Neurosci 17:3157–3167.
Nakashiba T, Young JZ, McHugh TJ, Buhl DL, Tonegawa S (2008) Transgenic inhibition of synaptic transmission reveals role of CA3 output in hippocampal learning. Science 319:1260–1264.
Nakazawa K, Quirk MC, Chitwood RA, Watanabe M, Yeckel MF, Sun LD, Kato A, Carr CA, Johnston D, Wilson MA, Tonegawa S (2002) Requirement for hippocampal CA3 NMDA receptors in associative memory recall. Science 297:211–218.
Nakazawa K, Sun LD, Quirk MC, Rondi-Reig L, Wilson MA, Tonegawa S (2003) Hippocampal CA3 NMDA receptors are crucial for memory acquisition of one-time experience. Neuron 38:305–315.
Neu A, Földy C, Soltesz I (2007) Postsynaptic origin of CB1-dependent tonic inhibition of GABA release at CCK-positive basket cell to pyramidal cell synapses in the CA1 region of the rat hippocampus. J Physiol 578:233–247.
Nitz D, McNaughton B (2004) Differential modulation of CA1 and dentate gyrus interneurons during exploration of novel environments. J Neurophysiol 91:863–872.
Nunzi MG, Gorio A, Milan F, Freund TF, Somogyi P, Smith AD (1985) Cholecystokinin-immunoreactive cells form symmetrical synaptic contacts with pyramidal and nonpyramidal neurons in the hippocampus. J Comp Neurol 237:485–505.
O'Keefe J, Dostrovsky J (1971) The hippocampus as a spatial map. Preliminary evidence from unit activity in the freely-moving rat. Brain Res 34:171–175.
O'Reilly RC, McClelland JL (1994) Hippocampal conjunctive encoding, storage, and recall: avoiding a trade-off. Hippocampus 4:661–682.
Pawelzik H, Hughes DI, Thomson AM (2002) Physiological and morphological diversity of immunocytochemically defined parvalbumin- and cholecystokinin-positive interneurones in CA1 of the adult rat hippocampus. J Comp Neurol 443:346–367.
Penttonen M, Kamondi A, Acsády L, Buzsáki G (1998) Gamma frequency oscillation in the hippocampus of the rat: intracellular analysis in vivo. Eur J Neurosci 10:718–728.
Pinault D (1996) A novel single-cell staining procedure performed in vivo under electrophysiological control: morpho-functional features of juxtacellularly labeled thalamic cells and other central neurons with biocytin or neurobiotin. J Neurosci Methods 65:113–136.
Pitler TA, Alger BE (1992) Postsynaptic spike firing reduces synaptic GABAA responses in hippocampal pyramidal cells. J Neurosci 12:4122–4132.
Puighermanal E, Marsicano G, Busquets-Garcia A, Lutz B, Maldonado R, Ozaita A (2009) Cannabinoid modulation of hippocampal long-term memory is mediated by mTOR signaling. Nat Neurosci 12:1152–1158.
Quilichini P, Sirota A, Buzsáki G (2010) Intrinsic circuit organization and theta-gamma oscillation dynamics in the entorhinal cortex of the rat. J Neurosci 30:11128–11142.
Ramon y Cajal S (1893) Estructura del asta de ammon y fascia dentata. Anal Soc Espan Historia Natural 22:53–114.
Robbe D, Buzsáki G (2009) Alteration of theta timescale dynamics of hippocampal place cells by a cannabinoid is associated with memory impairment. J Neurosci 29:12597–12605.
Robbe D, Montgomery SM, Thome A, Rueda-Orozco PE, McNaughton BL, Buzsaki G (2006) Cannabinoids reveal importance of spike timing coordination in hippocampal function. Nat Neurosci 9:1526–1533.
Rueda-Orozco PE, Soria-Gomez E, Montes-Rodriguez CJ, Martinez-Vargas M, Galicia O, Navarro L, Prospero-Garcia O (2008) A potential function of endocannabinoids in the selection of a navigation strategy by rats. Psychopharmacology (Berl) 198:565–576.
Scanziani M, Capogna M, Gähwiler BH, Thompson SM (1992) Presynaptic inhibition of miniature excitatory synaptic currents by baclofen and adenosine in the hippocampus. Neuron 9:919–927.
Schwaller B, Brückner G, Celio MR, Härtig W (1999) A polyclonal goat antiserum against the calcium-binding protein calretinin is a versatile tool for various immunochemical techniques. J Neurosci Methods 92:137–144.
Scoville WB, Milner B (1957) Loss of recent memory after bilateral hippocampal lesions. J Neurol Neurosurg Psychiatry 20:11–21.
Shigemoto R, Kulik A, Roberts JD, Ohishi H, Nusser Z, Kaneko T, Somogyi P (1996) Target-cell-specific concentration of a metabotropic glutamate receptor in the presynaptic active zone. Nature 381:523–525.
Sik A, Ylinen A, Penttonen M, Buzsáki G (1994) Inhibitory CA1-CA3-hilar region feedback in the hippocampus. Science 265:1722–1724.
Skaggs WE, McNaughton BL, Wilson MA, Barnes CA (1996) Theta phase precession in hippocampal neuronal populations and the compression of temporal sequences. Hippocampus 6:149–172.
Somogyi J, Baude A, Omori Y, Shimizu H, El Mestikawy S, Fukaya M, Shigemoto R, Watanabe M, Somogyi P (2004) GABAergic basket cells expressing cholecystokinin contain vesicular glutamate transporter type 3 (VGLUT3) in their synaptic terminals in hippocampus and isocortex of the rat. Eur J Neurosci 19:552–569.
Szabadics J, Soltesz I (2009) Functional Specificity of Mossy Fiber Innervation of GABAergic Cells in the Hippocampus. J Neurosci 29:4239–4251.
Szabó GG, Holderith N, Gulyás AI, Freund TF, Hájos N (2010) Distinct synaptic properties of perisomatic inhibitory cell types and their different modulation by cholinergic receptor activation in the CA3 region of the mouse hippocampus. Eur J Neurosci 31:2234–2246.
Tort AB, Komorowski RW, Manns JR, Kopell NJ, Eichenbaum H (2009) Theta-gamma coupling increases during the learning of item-context associations. Proc Natl Acad Sci U S A 106:20942–20947.
Treves A, Rolls ET (1992) Computational constraints suggest the need for two distinct input systems to the hippocampal CA3 network. Hippocampus 2:189–199.
Treves A, Rolls ET (1994) Computational analysis of the role of the hippocampus in memory. Hippocampus 4:374–391.
Tukker JJ, Fuentealba P, Hartwich K, Somogyi P, Klausberger T (2007) Cell type-specific tuning of hippocampal interneuron firing during gamma oscillations *in vivo*. J Neurosci 27:8184–8189.
Turner DA, Li XG, Pyapali GK, Ylinen A, Buzsaki G (1995) Morphometric and electrical properties of reconstructed hippocampal CA3 neurons recorded in vivo. J Comp Neurol 356:580–594.
Vanderwolf CH (1969) Hippocampal electrical activity and voluntary movement in the rat. Electroencephalogr Clin Neurophysiol 26:407–418.
Varga V, Losonczy A, Zemelman BV, Borhegyi Z, Nyiri G, Domonkos A, Hangya B, Holderith N, Magee JC, Freund TF (2009) Fast synaptic subcortical control of hippocampal circuits. Science 326:449–453.
Varvel SA, Anum E, Niyuhire F, Wise LE, Lichtman AH (2005) Delta(9)-THC-induced cognitive deficits in mice are reversed by the $GABA_A$ antagonist bicuculline. Psychopharmacology (Berl) 178:317–327.
Vida I, Frotscher M (2000) A hippocampal interneuron associated with the mossy fiber system. Proc Natl Acad Sci U S A 97:1275–1280.
Wilson MA, McNaughton BL (1993) Dynamics of the hippocampal ensemble code for space. Science 261:1055–1058.
Wilson RI, Nicoll RA (2001) Endogenous cannabinoids mediate retrograde signalling at hippocampal synapses. Nature 410:588–592.
Wood ER, Dudchenko PA, Eichenbaum H (1999) The global record of memory in hippocampal neuronal activity. Nature 397:613–616.
Ylinen A, Bragin A, Nádasdy Z, Jandó G, Szabó I, Sik A, Buzsáki G (1995) Sharp wave-associated high-frequency oscillation (200 Hz) in the intact hippocampus: network and intracellular mechanisms. J Neurosci 15:30–46.
Zar JH (1999) Biostatistical analysis. New Jersey: Prentice-Hall.